



CERN-PH-EP-2013-074

LHCb-PAPER-2013-019

April 23, 2013

Differential branching fraction and angular analysis of the decay $B^0 \rightarrow K^{*0} \mu^+ \mu^-$

The LHCb collaboration[†]

Abstract

The angular distribution and differential branching fraction of the decay $B^0 \rightarrow K^{*0} \mu^+ \mu^-$ are studied using a data sample, collected by the LHCb experiment in pp collisions at $\sqrt{s} = 7$ TeV, corresponding to an integrated luminosity of 1.0 fb^{-1} . Several angular observables are measured in bins of the dimuon invariant mass squared, q^2 . A first measurement of the zero-crossing point of the forward-backward asymmetry of the dimuon system is also presented. The zero-crossing point is measured to be $q_0^2 = 4.9 \pm 0.9 \text{ GeV}^2/c^4$, where the uncertainty is the sum of statistical and systematic uncertainties. The results are consistent with the Standard Model predictions.

Submitted to JHEP

© CERN on behalf of the LHCb collaboration, license CC-BY-3.0.

[†]Authors are listed on the following pages.

LHCb collaboration

R. Aaij⁴⁰, C. Abellan Beteta^{35,n}, B. Adeva³⁶, M. Adinolfi⁴⁵, C. Adrover⁶, A. Affolder⁵¹,
 Z. Ajaltouni⁵, J. Albrecht⁹, F. Alessio³⁷, M. Alexander⁵⁰, S. Ali⁴⁰, G. Alkhazov²⁹,
 P. Alvarez Cartelle³⁶, A.A. Alves Jr^{24,37}, S. Amato², S. Amerio²¹, Y. Amhis⁷, L. Anderlini^{17,f},
 J. Anderson³⁹, R. Andreassen⁵⁶, R.B. Appleby⁵³, O. Aquines Gutierrez¹⁰, F. Archilli¹⁸,
 A. Artamonov³⁴, M. Artuso⁵⁸, E. Aslanides⁶, G. Auriemma^{24,m}, S. Bachmann¹¹, J.J. Back⁴⁷,
 C. Baesso⁵⁹, V. Balagura³⁰, W. Baldini¹⁶, R.J. Barlow⁵³, C. Barschel³⁷, S. Barsuk⁷,
 W. Barter⁴⁶, Th. Bauer⁴⁰, A. Bay³⁸, J. Beddow⁵⁰, F. Bedeschi²², I. Bediaga¹, S. Belogurov³⁰,
 K. Belous³⁴, I. Belyaev³⁰, E. Ben-Haim⁸, G. Bencivenni¹⁸, S. Benson⁴⁹, J. Benton⁴⁵,
 A. Berezhnoy³¹, R. Bernet³⁹, M.-O. Bettler⁴⁶, M. van Beuzekom⁴⁰, A. Bien¹¹, S. Bifani⁴⁴,
 T. Bird⁵³, A. Bizzeti^{17,h}, P.M. Bjørnstad⁵³, T. Blake³⁷, F. Blanc³⁸, J. Blouw¹¹, S. Blusk⁵⁸,
 V. Bocci²⁴, A. Bondar³³, N. Bondar²⁹, W. Bonivento¹⁵, S. Borghi⁵³, A. Borgia⁵⁸,
 T.J.V. Bowcock⁵¹, E. Bowen³⁹, C. Bozzi¹⁶, T. Brambach⁹, J. van den Brand⁴¹, J. Bressieux³⁸,
 D. Brett⁵³, M. Britsch¹⁰, T. Britton⁵⁸, N.H. Brook⁴⁵, H. Brown⁵¹, I. Burducea²⁸, A. Bursche³⁹,
 G. Busetto^{21,q}, J. Buytaert³⁷, S. Cadeddu¹⁵, O. Callot⁷, M. Calvi^{20,j}, M. Calvo Gomez^{35,n},
 A. Camboni³⁵, P. Campana^{18,37}, D. Campora Perez³⁷, A. Carbone^{14,c}, G. Carboni^{23,k},
 R. Cardinale^{19,i}, A. Cardini¹⁵, H. Carranza-Mejia⁴⁹, L. Carson⁵², K. Carvalho Akiba²,
 G. Casse⁵¹, L. Castillo Garcia³⁷, M. Cattaneo³⁷, Ch. Cauet⁹, M. Charles⁵⁴, Ph. Charpentier³⁷,
 P. Chen^{3,38}, N. Chiapolini³⁹, M. Chrzasczcz²⁵, K. Ciba³⁷, X. Cid Vidal³⁷, G. Ciezarek⁵²,
 P.E.L. Clarke⁴⁹, M. Clemencic³⁷, H.V. Cliff⁴⁶, J. Closier³⁷, C. Coca²⁸, V. Coco⁴⁰, J. Cogan⁶,
 E. Cogneras⁵, P. Collins³⁷, A. Comerma-Montells³⁵, A. Contu^{15,37}, A. Cook⁴⁵, M. Coombes⁴⁵,
 S. Coquereau⁸, G. Corti³⁷, B. Couturier³⁷, G.A. Cowan⁴⁹, D.C. Craik⁴⁷, S. Cunliffe⁵²,
 R. Currie⁴⁹, C. D'Ambrosio³⁷, P. David⁸, P.N.Y. David⁴⁰, A. Davis⁵⁶, I. De Bonis⁴,
 K. De Bruyn⁴⁰, S. De Capua⁵³, M. De Cian³⁹, J.M. De Miranda¹, L. De Paula², W. De Silva⁵⁶,
 P. De Simone¹⁸, D. Decamp⁴, M. Deckenhoff⁹, L. Del Buono⁸, N. Deléage⁴, D. Derkach¹⁴,
 O. Deschamps⁵, F. Dettori⁴¹, A. Di Canto¹¹, F. Di Ruscio^{23,k}, H. Dijkstra³⁷, M. Dogaru²⁸,
 S. Donleavy⁵¹, F. Dordei¹¹, A. Dosil Suárez³⁶, D. Dossett⁴⁷, A. Dovbnya⁴², F. Dupertuis³⁸,
 R. Dzhelyadin³⁴, A. Dziurda²⁵, A. Dzyuba²⁹, S. Easo^{48,37}, U. Egede⁵², V. Egorychev³⁰,
 S. Eidelman³³, D. van Eijk⁴⁰, S. Eisenhardt⁴⁹, U. Eitschberger⁹, R. Ekelhof⁹, L. Eklund^{50,37},
 I. El Rifai⁵, Ch. Elsasser³⁹, D. Elsby⁴⁴, A. Falabella^{14,e}, C. Färber¹¹, G. Fardell⁴⁹, C. Farinelli⁴⁰,
 S. Farry¹², V. Fave³⁸, D. Ferguson⁴⁹, V. Fernandez Albor³⁶, F. Ferreira Rodrigues¹,
 M. Ferro-Luzzi³⁷, S. Filippov³², M. Fiore¹⁶, C. Fitzpatrick³⁷, M. Fontana¹⁰, F. Fontanelli^{19,i},
 R. Forty³⁷, O. Francisco², M. Frank³⁷, C. Frei³⁷, M. Frosini^{17,f}, S. Furcas²⁰, E. Furfaro^{23,k},
 A. Gallas Torreira³⁶, D. Galli^{14,c}, M. Gandelman², P. Gandini⁵⁸, Y. Gao³, J. Garofoli⁵⁸,
 P. Garosi⁵³, J. Garra Tico⁴⁶, L. Garrido³⁵, C. Gaspar³⁷, R. Gauld⁵⁴, E. Gersabeck¹¹,
 M. Gersabeck⁵³, T. Gershon^{47,37}, Ph. Ghez⁴, V. Gibson⁴⁶, V.V. Gligorov³⁷, C. Göbel⁵⁹,
 D. Golubkov³⁰, A. Golutvin^{52,30,37}, A. Gomes², H. Gordon⁵⁴, M. Grabalosa Gándara⁵,
 R. Graciani Diaz³⁵, L.A. Granado Cardoso³⁷, E. Graugés³⁵, G. Graziani¹⁷, A. Grecu²⁸,
 E. Greening⁵⁴, S. Gregson⁴⁶, P. Griffith⁴⁴, O. Grünberg⁶⁰, B. Gui⁵⁸, E. Gushchin³², Yu. Guz^{34,37},
 T. Gys³⁷, C. Hadjivasiliou⁵⁸, G. Haefeli³⁸, C. Haen³⁷, S.C. Haines⁴⁶, S. Hall⁵², T. Hampson⁴⁵,
 S. Hansmann-Menzemer¹¹, N. Harnew⁵⁴, S.T. Harnew⁴⁵, J. Harrison⁵³, T. Hartmann⁶⁰, J. He³⁷,
 V. Heijne⁴⁰, K. Hennessy⁵¹, P. Henrard⁵, J.A. Hernando Morata³⁶, E. van Herwijnen³⁷,
 E. Hicks⁵¹, D. Hill⁵⁴, M. Hoballah⁵, C. Hombach⁵³, P. Hopchev⁴, W. Hulsbergen⁴⁰, P. Hunt⁵⁴,
 T. Huse⁵¹, N. Hussain⁵⁴, D. Hutchcroft⁵¹, D. Hynds⁵⁰, V. Iakovenko⁴³, M. Idzik²⁶, P. Ilten¹²,
 R. Jacobsson³⁷, A. Jaeger¹¹, E. Jans⁴⁰, P. Jaton³⁸, A. Jawahery⁵⁷, F. Jing³, M. John⁵⁴,

D. Johnson⁵⁴, C.R. Jones⁴⁶, C. Joram³⁷, B. Jost³⁷, M. Kaballo⁹, S. Kandybei⁴², M. Karacson³⁷,
T.M. Karbach³⁷, I.R. Kenyon⁴⁴, U. Kerzel³⁷, T. Ketel⁴¹, A. Keune³⁸, B. Khanji²⁰,
O. Kochebina⁷, I. Komarov³⁸, R.F. Koopman⁴¹, P. Koppenburg⁴⁰, M. Korolev³¹,
A. Kozlinskiy⁴⁰, L. Kravchuk³², K. Kreplin¹¹, M. Kreps⁴⁷, G. Krocker¹¹, P. Krokovny³³,
F. Kruse⁹, M. Kucharczyk^{20,25,j}, V. Kudryavtsev³³, T. Kvaratskheliya^{30,37}, V.N. La Thi³⁸,
D. Lacarrere³⁷, G. Lafferty⁵³, A. Lai¹⁵, D. Lambert⁴⁹, R.W. Lambert⁴¹, E. Lanciotti³⁷,
G. Lanfranchi¹⁸, C. Langenbruch³⁷, T. Latham⁴⁷, C. Lazzeroni⁴⁴, R. Le Gac⁶, J. van Leerdam⁴⁰,
J.-P. Lees⁴, R. Lefèvre⁵, A. Leflat³¹, J. Lefrançois⁷, S. Leo²², O. Leroy⁶, T. Lesiak²⁵,
B. Leverington¹¹, Y. Li³, L. Li Gioi⁵, M. Liles⁵¹, R. Lindner³⁷, C. Linn¹¹, B. Liu³, G. Liu³⁷,
S. Lohn³⁷, I. Longstaff⁵⁰, J.H. Lopes², E. Lopez Asamar³⁵, N. Lopez-March³⁸, H. Lu³,
D. Lucchesi^{21,q}, J. Luisier³⁸, H. Luo⁴⁹, F. Machefert⁷, I.V. Machikhiliyan^{4,30}, F. Maciuc²⁸,
O. Maev^{29,37}, S. Malde⁵⁴, G. Manca^{15,d}, G. Mancinelli⁶, U. Marconi¹⁴, R. Märki³⁸, J. Marks¹¹,
G. Martellotti²⁴, A. Martens⁸, L. Martin⁵⁴, A. Martín Sánchez⁷, M. Martinelli⁴⁰,
D. Martinez Santos⁴¹, D. Martins Tostes², A. Massafferri¹, R. Matev³⁷, Z. Mathe³⁷,
C. Matteuzzi²⁰, E. Maurice⁶, A. Mazurov^{16,32,37,e}, J. McCarthy⁴⁴, A. McNab⁵³, R. McNulty¹²,
B. Meadows^{56,54}, F. Meier⁹, M. Meissner¹¹, M. Merk⁴⁰, D.A. Milanes⁸, M.-N. Minard⁴,
J. Molina Rodriguez⁵⁹, S. Monteil⁵, D. Moran⁵³, P. Morawski²⁵, M.J. Morello^{22,s},
R. Mountain⁵⁸, I. Mous⁴⁰, F. Muheim⁴⁹, K. Müller³⁹, R. Muresan²⁸, B. Muryn²⁶, B. Muster³⁸,
P. Naik⁴⁵, T. Nakada³⁸, R. Nandakumar⁴⁸, I. Nasteva¹, M. Needham⁴⁹, N. Neufeld³⁷,
A.D. Nguyen³⁸, T.D. Nguyen³⁸, C. Nguyen-Mau^{38,p}, M. Nicol⁷, V. Niess⁵, R. Niet⁹, N. Nikitin³¹,
T. Nikodem¹¹, A. Nomerotski⁵⁴, A. Novoselov³⁴, A. Oblakowska-Mucha²⁶, V. Obraztsov³⁴,
S. Oggero⁴⁰, S. Ogilvy⁵⁰, O. Okhrimenko⁴³, R. Oldeman^{15,d}, M. Orlandea²⁸,
J.M. Otalora Goicochea², P. Owen⁵², A. Oyanguren^{35,o}, B.K. Pal⁵⁸, A. Palano^{13,b},
M. Palutan¹⁸, J. Panman³⁷, A. Papanestis⁴⁸, M. Pappagallo⁵⁰, C. Parkes⁵³, C.J. Parkinson⁵²,
G. Passaleva¹⁷, G.D. Patel⁵¹, M. Patel⁵², G.N. Patrick⁴⁸, C. Patrignani^{19,i}, C. Pavel-Nicorescu²⁸,
A. Pazos Alvarez³⁶, A. Pellegrino⁴⁰, G. Penso^{24,l}, M. Pepe Altarelli³⁷, S. Perazzini^{14,c},
D.L. Perego^{20,j}, E. Perez Trigo³⁶, A. Pérez-Calero Yzquierdo³⁵, P. Perret⁵, M. Perrin-Terrin⁶,
G. Pessina²⁰, K. Petridis⁵², A. Petrolini^{19,i}, A. Phan⁵⁸, E. Picatoste Olloqui³⁵, B. Pietrzyk⁴,
T. Pilař⁴⁷, D. Pinci²⁴, S. Playfer⁴⁹, M. Plo Casasus³⁶, F. Polci⁸, G. Polok²⁵, A. Poluektov^{47,33},
E. Polcarpo², A. Popov³⁴, D. Popov¹⁰, B. Popovici²⁸, C. Potterat³⁵, A. Powell⁵⁴,
J. Prisciandaro³⁸, V. Pugatch⁴³, A. Puig Navarro³⁸, G. Punzi^{22,r}, W. Qian⁴, J.H. Rademacker⁴⁵,
B. Rakotomiamanana³⁸, M.S. Rangel², I. Raniuk⁴², N. Rauschmayr³⁷, G. Raven⁴¹,
S. Redford⁵⁴, M.M. Reid⁴⁷, A.C. dos Reis¹, S. Ricciardi⁴⁸, A. Richards⁵², K. Rinnert⁵¹,
V. Rives Molina³⁵, D.A. Roa Romero⁵, P. Robbe⁷, E. Rodrigues⁵³, P. Rodriguez Perez³⁶,
S. Roiser³⁷, V. Romanovsky³⁴, A. Romero Vidal³⁶, J. Rouvinet³⁸, T. Ruf³⁷, F. Ruffini²²,
H. Ruiz³⁵, P. Ruiz Valls^{35,o}, G. Sabatino^{24,k}, J.J. Saborido Silva³⁶, N. Sagidova²⁹, P. Sail⁵⁰,
B. Saitta^{15,d}, V. Salustino Guimaraes², C. Salzmann³⁹, B. Sanmartin Sedes³⁶, M. Sannino^{19,i},
R. Santacesaria²⁴, C. Santamarina Rios³⁶, E. Santovetti^{23,k}, M. Sapunov⁶, A. Sarti^{18,l},
C. Satriano^{24,m}, A. Satta²³, M. Savrie^{16,e}, D. Savrina^{30,31}, P. Schaack⁵², M. Schiller⁴¹,
H. Schindler³⁷, M. Schlupp⁹, M. Schmelling¹⁰, B. Schmidt³⁷, O. Schneider³⁸, A. Schopper³⁷,
M.-H. Schune⁷, R. Schwemmer³⁷, B. Sciascia¹⁸, A. Sciubba²⁴, M. Seco³⁶, A. Semennikov³⁰,
K. Senderowska²⁶, I. Sepp⁵², N. Serra³⁹, J. Serrano⁶, P. Seyfert¹¹, M. Shapkin³⁴,
I. Shapoval^{16,42}, P. Shatalov³⁰, Y. Shcheglov²⁹, T. Shears^{51,37}, L. Shekhtman³³, O. Shevchenko⁴²,
V. Shevchenko³⁰, A. Shires⁵², R. Silva Coutinho⁴⁷, T. Skwarnicki⁵⁸, N.A. Smith⁵¹, E. Smith^{54,48},
M. Smith⁵³, M.D. Sokoloff⁵⁶, F.J.P. Soler⁵⁰, F. Soomro¹⁸, D. Souza⁴⁵, B. Souza De Paula²,
B. Spaan⁹, A. Sparkes⁴⁹, P. Spradlin⁵⁰, F. Stagni³⁷, S. Stahl¹¹, O. Steinkamp³⁹, S. Stoica²⁸,

S. Stone⁵⁸, B. Storaci³⁹, M. Straticiuc²⁸, U. Straumann³⁹, V.K. Subbiah³⁷, L. Sun⁵⁶,
S. Swientek⁹, V. Syropoulos⁴¹, M. Szczekowski²⁷, P. Szczypka^{38,37}, T. Szumlak²⁶, S. T’Jampens⁴,
M. Teklishyn⁷, E. Teodorescu²⁸, F. Teubert³⁷, C. Thomas⁵⁴, E. Thomas³⁷, J. van Tilburg¹¹,
V. Tisserand⁴, M. Tobin³⁸, S. Tolk⁴¹, D. Tonelli³⁷, S. Topp-Joergensen⁵⁴, N. Torr⁵⁴,
E. Tournefier^{4,52}, S. Tourneur³⁸, M.T. Tran³⁸, M. Tresch³⁹, A. Tsaregorodtsev⁶, P. Tsopelas⁴⁰,
N. Tuning⁴⁰, M. Ubeda Garcia³⁷, A. Ukleja²⁷, D. Urner⁵³, U. Uwer¹¹, V. Vagnoni¹⁴,
G. Valenti¹⁴, R. Vazquez Gomez³⁵, P. Vazquez Regueiro³⁶, S. Vecchi¹⁶, J.J. Velthuis⁴⁵,
M. Veltri^{17,9}, G. Veneziano³⁸, M. Vesterinen³⁷, B. Viaud⁷, D. Vieira², X. Vilasis-Cardona^{35,n},
A. Vollhardt³⁹, D. Volyanskyy¹⁰, D. Voong⁴⁵, A. Vorobyev²⁹, V. Vorobyev³³, C. Voß⁶⁰,
H. Voss¹⁰, R. Waldi⁶⁰, R. Wallace¹², S. Wandernoth¹¹, J. Wang⁵⁸, D.R. Ward⁴⁶, N.K. Watson⁴⁴,
A.D. Webber⁵³, D. Websdale⁵², M. Whitehead⁴⁷, J. Wicht³⁷, J. Wiechczynski²⁵, D. Wiedner¹¹,
L. Wiggers⁴⁰, G. Wilkinson⁵⁴, M.P. Williams^{47,48}, M. Williams⁵⁵, F.F. Wilson⁴⁸, J. Wishahi⁹,
M. Witek²⁵, S.A. Wotton⁴⁶, S. Wright⁴⁶, S. Wu³, K. Wyllie³⁷, Y. Xie^{49,37}, F. Xing⁵⁴, Z. Xing⁵⁸,
Z. Yang³, R. Young⁴⁹, X. Yuan³, O. Yushchenko³⁴, M. Zangoli¹⁴, M. Zavertyaev^{10,a}, F. Zhang³,
L. Zhang⁵⁸, W.C. Zhang¹², Y. Zhang³, A. Zhelezov¹¹, A. Zhokhov³⁰, L. Zhong³, A. Zvyagin³⁷.

¹ Centro Brasileiro de Pesquisas Físicas (CBPF), Rio de Janeiro, Brazil

² Universidade Federal do Rio de Janeiro (UFRJ), Rio de Janeiro, Brazil

³ Center for High Energy Physics, Tsinghua University, Beijing, China

⁴ LAPP, Université de Savoie, CNRS/IN2P3, Annecy-Le-Vieux, France

⁵ Clermont Université, Université Blaise Pascal, CNRS/IN2P3, LPC, Clermont-Ferrand, France

⁶ CPPM, Aix-Marseille Université, CNRS/IN2P3, Marseille, France

⁷ LAL, Université Paris-Sud, CNRS/IN2P3, Orsay, France

⁸ LPNHE, Université Pierre et Marie Curie, Université Paris Diderot, CNRS/IN2P3, Paris, France

⁹ Fakultät Physik, Technische Universität Dortmund, Dortmund, Germany

¹⁰ Max-Planck-Institut für Kernphysik (MPIK), Heidelberg, Germany

¹¹ Physikalisches Institut, Ruprecht-Karls-Universität Heidelberg, Heidelberg, Germany

¹² School of Physics, University College Dublin, Dublin, Ireland

¹³ Sezione INFN di Bari, Bari, Italy

¹⁴ Sezione INFN di Bologna, Bologna, Italy

¹⁵ Sezione INFN di Cagliari, Cagliari, Italy

¹⁶ Sezione INFN di Ferrara, Ferrara, Italy

¹⁷ Sezione INFN di Firenze, Firenze, Italy

¹⁸ Laboratori Nazionali dell’INFN di Frascati, Frascati, Italy

¹⁹ Sezione INFN di Genova, Genova, Italy

²⁰ Sezione INFN di Milano Bicocca, Milano, Italy

²¹ Sezione INFN di Padova, Padova, Italy

²² Sezione INFN di Pisa, Pisa, Italy

²³ Sezione INFN di Roma Tor Vergata, Roma, Italy

²⁴ Sezione INFN di Roma La Sapienza, Roma, Italy

²⁵ Henryk Niewodniczanski Institute of Nuclear Physics Polish Academy of Sciences, Kraków, Poland

²⁶ AGH - University of Science and Technology, Faculty of Physics and Applied Computer Science, Kraków, Poland

²⁷ National Center for Nuclear Research (NCBJ), Warsaw, Poland

²⁸ Horia Hulubei National Institute of Physics and Nuclear Engineering, Bucharest-Magurele, Romania

²⁹ Petersburg Nuclear Physics Institute (PNPI), Gatchina, Russia

³⁰ Institute of Theoretical and Experimental Physics (ITEP), Moscow, Russia

³¹ Institute of Nuclear Physics, Moscow State University (SINP MSU), Moscow, Russia

³² Institute for Nuclear Research of the Russian Academy of Sciences (INR RAN), Moscow, Russia

³³ Budker Institute of Nuclear Physics (SB RAS) and Novosibirsk State University, Novosibirsk, Russia

- ³⁴*Institute for High Energy Physics (IHEP), Protvino, Russia*
- ³⁵*Universitat de Barcelona, Barcelona, Spain*
- ³⁶*Universidad de Santiago de Compostela, Santiago de Compostela, Spain*
- ³⁷*European Organization for Nuclear Research (CERN), Geneva, Switzerland*
- ³⁸*Ecole Polytechnique Fédérale de Lausanne (EPFL), Lausanne, Switzerland*
- ³⁹*Physik-Institut, Universität Zürich, Zürich, Switzerland*
- ⁴⁰*Nikhef National Institute for Subatomic Physics, Amsterdam, The Netherlands*
- ⁴¹*Nikhef National Institute for Subatomic Physics and VU University Amsterdam, Amsterdam, The Netherlands*
- ⁴²*NSC Kharkiv Institute of Physics and Technology (NSC KIPT), Kharkiv, Ukraine*
- ⁴³*Institute for Nuclear Research of the National Academy of Sciences (KINR), Kyiv, Ukraine*
- ⁴⁴*University of Birmingham, Birmingham, United Kingdom*
- ⁴⁵*H.H. Wills Physics Laboratory, University of Bristol, Bristol, United Kingdom*
- ⁴⁶*Cavendish Laboratory, University of Cambridge, Cambridge, United Kingdom*
- ⁴⁷*Department of Physics, University of Warwick, Coventry, United Kingdom*
- ⁴⁸*STFC Rutherford Appleton Laboratory, Didcot, United Kingdom*
- ⁴⁹*School of Physics and Astronomy, University of Edinburgh, Edinburgh, United Kingdom*
- ⁵⁰*School of Physics and Astronomy, University of Glasgow, Glasgow, United Kingdom*
- ⁵¹*Oliver Lodge Laboratory, University of Liverpool, Liverpool, United Kingdom*
- ⁵²*Imperial College London, London, United Kingdom*
- ⁵³*School of Physics and Astronomy, University of Manchester, Manchester, United Kingdom*
- ⁵⁴*Department of Physics, University of Oxford, Oxford, United Kingdom*
- ⁵⁵*Massachusetts Institute of Technology, Cambridge, MA, United States*
- ⁵⁶*University of Cincinnati, Cincinnati, OH, United States*
- ⁵⁷*University of Maryland, College Park, MD, United States*
- ⁵⁸*Syracuse University, Syracuse, NY, United States*
- ⁵⁹*Pontifícia Universidade Católica do Rio de Janeiro (PUC-Rio), Rio de Janeiro, Brazil, associated to ²*
- ⁶⁰*Institut für Physik, Universität Rostock, Rostock, Germany, associated to ¹¹*
- ^a*P.N. Lebedev Physical Institute, Russian Academy of Science (LPI RAS), Moscow, Russia*
- ^b*Università di Bari, Bari, Italy*
- ^c*Università di Bologna, Bologna, Italy*
- ^d*Università di Cagliari, Cagliari, Italy*
- ^e*Università di Ferrara, Ferrara, Italy*
- ^f*Università di Firenze, Firenze, Italy*
- ^g*Università di Urbino, Urbino, Italy*
- ^h*Università di Modena e Reggio Emilia, Modena, Italy*
- ⁱ*Università di Genova, Genova, Italy*
- ^j*Università di Milano Bicocca, Milano, Italy*
- ^k*Università di Roma Tor Vergata, Roma, Italy*
- ^l*Università di Roma La Sapienza, Roma, Italy*
- ^m*Università della Basilicata, Potenza, Italy*
- ⁿ*LIFAEELS, La Salle, Universitat Ramon Llull, Barcelona, Spain*
- ^o*IFIC, Universitat de Valencia-CSIC, Valencia, Spain*
- ^p*Hanoi University of Science, Hanoi, Viet Nam*
- ^q*Università di Padova, Padova, Italy*
- ^r*Università di Pisa, Pisa, Italy*
- ^s*Scuola Normale Superiore, Pisa, Italy*

1 Introduction

The $B^0 \rightarrow K^{*0} \mu^+ \mu^-$ decay,¹ where $K^{*0} \rightarrow K^+ \pi^-$, is a $b \rightarrow s$ flavour changing neutral current process that is mediated by electroweak box and penguin type diagrams in the Standard Model (SM). The angular distribution of the $K^+ \pi^- \mu^+ \mu^-$ system offers particular sensitivity to contributions from new particles in extensions to the SM. The differential branching fraction of the decay also provides information on the contribution from those new particles but typically suffers from larger theoretical uncertainties due to hadronic form factors.

The angular distribution of the decay can be described by three angles (θ_ℓ, θ_K and ϕ) and by the invariant mass squared of the dimuon system (q^2). The $B^0 \rightarrow K^{*0} \mu^+ \mu^-$ decay is self-tagging through the charge of the kaon and so there is some freedom in the choice of the angular basis that is used to describe the decay. In this paper, the angle θ_ℓ is defined as the angle between the direction of the μ^+ (μ^-) in the dimuon rest frame and the direction of the dimuon in the B^0 (\bar{B}^0) rest frame. The angle θ_K is defined as the angle between the direction of the kaon in the K^{*0} (\bar{K}^{*0}) rest frame and the direction of the K^{*0} (\bar{K}^{*0}) in the B^0 (\bar{B}^0) rest frame. The angle ϕ is the angle between the plane containing the μ^+ and μ^- and the plane containing the kaon and pion from the K^{*0} . A detailed description of the angular basis is given in Appendix A. In this basis, the angular definition for the \bar{B}^0 decay is a CP transformation of that for the B^0 decay.

Using the notation of Ref. [1], and assuming equal numbers of B^0 and \bar{B}^0 decays, the differential decay rate corresponds to

$$\frac{1}{d\Gamma/dq^2} \frac{d^4\Gamma}{dq^2 d\cos\theta_\ell d\cos\theta_K d\phi} = \frac{9}{32\pi} \left[S_1^s \sin^2 \theta_K + S_1^c \cos^2 \theta_K + \right. \\ S_2^s \sin^2 \theta_K \cos 2\theta_\ell + S_2^c \cos^2 \theta_K \cos 2\theta_\ell + \\ S_3 \sin^2 \theta_K \sin^2 \theta_\ell \cos 2\phi + S_4 \sin 2\theta_K \sin 2\theta_\ell \cos \phi + \\ S_5 \sin 2\theta_K \sin \theta_\ell \cos \phi + S_6 \sin^2 \theta_K \cos \theta_\ell + \\ S_7 \sin 2\theta_K \sin \theta_\ell \sin \phi + S_8 \sin 2\theta_K \sin 2\theta_\ell \sin \phi + \\ \left. S_9 \sin^2 \theta_K \sin^2 \theta_\ell \sin 2\phi \right], \quad (1)$$

where the S_i terms are CP averages between B^0 and \bar{B}^0 of bilinear combinations of K^{*0} decay amplitudes that vary with q^2 . The terms S_7 , S_8 and S_9 are suppressed by the small size of the strong phase difference between the amplitudes involved and are expected to be close to zero across the full q^2 range not only in the SM but also in most extensions. To reveal the effect of new particles, it is better to look instead at the corresponding CP asymmetries A_7 , A_8 and A_9 , between B^0 and \bar{B}^0 , which are not suppressed by the size of

¹Charge conjugation is implied throughout this paper unless stated otherwise.

the strong phases involved [2]. This is achieved by flipping the sign of ϕ for the \bar{B}^0 decay in Eq. 1, replacing S_7 , S_8 and S_9 by A_7 , A_8 and A_9 .

If $q^2 \gg 4m_\mu^2$ (where m_μ is the muon mass), the terms S_1^c , S_1^s , S_2^c and S_2^s in Eq. 1 are related to the fraction of longitudinal polarisation of the K^{*0} meson, F_L ($S_1^c = -S_2^c = F_L$ and $\frac{4}{3}S_1^s = 4S_2^s = 1 - F_L$). The angular term $\sin^2 \theta_K \cos \theta_\ell$ is responsible for generating the forward-backward asymmetry of the dimuon system, A_{FB} [3] ($A_{\text{FB}} = \frac{3}{4}S_6$). The term S_3 is proportional to the asymmetry between the two transverse K^{*0} amplitudes, A_T^2 [4].

Due to the limited number of signal candidates that are available in the present analysis, the angle ϕ is also transformed such that

$$\hat{\phi} = \begin{cases} \phi + \pi & \text{if } \phi < 0 \\ \phi & \text{otherwise} \end{cases} \quad (2)$$

to cancel terms in Eq. 1 that have either a $\sin \phi$ or a $\cos \phi$ dependence and provide a simplified angular expression. The reduced angular expression then contains only F_L , A_{FB} , S_3 and A_9 and is given in full in Sec. 7.

In the large-recoil (low q^2) limit, the observables A_T^2 and A_T^{Re} , where $S_3 = \frac{1}{2}(1 - F_L)A_T^2$ and $A_{\text{FB}} = \frac{3}{4}(1 - F_L)A_T^{\text{Re}}$, can be defined and have reduced form-factor uncertainties [4, 5]. The observables A_T^2 and A_T^{Re} depend only on the transverse decay amplitudes.

This paper presents a measurement of the differential branching fraction ($d\mathcal{B}/dq^2$), A_{FB} , F_L , S_3 and A_9 of the $B^0 \rightarrow K^{*0}\mu^+\mu^-$ decay in six bins of q^2 . Measurements of the transverse asymmetries A_T^2 and A_T^{Re} are also presented. The analysis is based on a dataset, corresponding to 1.0 fb^{-1} of integrated luminosity, collected by the LHCb detector in $\sqrt{s} = 7 \text{ TeV}$ pp collisions in 2011. Section 2 describes the experimental setup used in the analyses. Section 3 describes the event selection. Section 4 discusses potential sources of peaking background. Section 5 describes the treatment of the detector acceptance in the analysis. Section 6 discusses the measurement of $d\mathcal{B}/dq^2$. The angular analysis of the decay, in terms of $\cos \theta_\ell$, $\cos \theta_K$ and $\hat{\phi}$, is described in Sec. 7. Finally, in the SM, A_{FB} varies as a function of q^2 and is known to change sign at a predictable value of q^2 . A first measurement of this zero-crossing point is presented in Sec. 8.

The one-dimensional $\cos \theta_\ell$, $\cos \theta_K$ and ϕ distributions have previously been studied at LHCb [6], BaBar [7], Belle [8] and CDF [9] with smaller data samples.

2 The LHCb detector

The LHCb detector [10] is a single-arm forward spectrometer, covering the pseudorapidity range $2 < \eta < 5$, that is designed to study b and c hadron decays. A dipole magnet with a bending power of 4 Tm and a large area tracking detector provide momentum resolution ranging from 0.4% for tracks with a momentum of 5 GeV/ c to 0.6% for a momentum of 100 GeV/ c . A silicon microstrip detector, located around the pp interaction region, provides excellent separation of B meson decay vertices from the primary pp interaction and impact parameter resolution of 20 μm for tracks with high transverse momentum (p_T). Two ring-imaging Cherenkov (RICH) detectors [11] provide kaon-pion separation in the

momentum range $2 - 100 \text{ GeV}/c$. Muons are identified based on hits created in a system of multiwire proportional chambers interleaved with layers of iron. The LHCb trigger [12] comprises a hardware trigger and a two-stage software trigger that performs a full event reconstruction.

Samples of simulated events are used to estimate the contribution from specific sources of exclusive backgrounds and the efficiency to trigger, reconstruct and select the $B^0 \rightarrow K^{*0} \mu^+ \mu^-$ signal. The simulated pp interactions are generated using PYTHIA 6.4 [13] with a specific LHCb configuration [14]. Decays of hadronic particles are then described by EVTGEN [15] in which final state radiation is generated using PHOTOS [16]. Finally, the GEANT4 toolkit [17] is used to simulate the detector response to the particles produced by PYTHIA/EVTGEN, as described in Ref. [18]. The simulated samples are corrected for known differences between data and simulation in the B^0 momentum spectrum, the detector impact parameter resolution, particle identification [11] and tracking system performance using control samples from the data.

3 Selection of signal candidates

The $B^0 \rightarrow K^{*0} \mu^+ \mu^-$ candidates are selected from events that have been triggered by a muon with $p_T > 1.5 \text{ GeV}/c$, in the hardware trigger. In the first stage of the software trigger, candidates are selected if there is a reconstructed track in the event with high impact parameter ($> 125 \mu\text{m}$) with respect to one of the primary pp interactions and $p_T > 1.5 \text{ GeV}/c$. In the second stage of the software trigger, candidates are triggered on the kinematic properties of the partially or fully reconstructed B^0 candidate [12].

Signal candidates are then required to pass a set of loose (pre-)selection requirements. Candidates are selected for further analysis if: the B^0 decay vertex is separated from the primary pp interaction; the B^0 candidate impact parameter is small, and the impact parameters of the charged kaon, pion and muons are large, with respect to the primary pp interaction; and the angle between the B^0 momentum vector and the vector between the primary pp interaction and the B^0 decay vertex is small. Candidates are retained if their $K^+ \pi^-$ invariant mass is in the range $792 < m(K^+ \pi^-) < 992 \text{ MeV}/c^2$.

A multivariate selection, using a boosted decision tree (BDT) [19] with the AdaBoost algorithm [20], is applied to further reduce the level of combinatorial background. The BDT is identical to that described in Ref. [6]. It has been trained on a data sample, corresponding to 36 pb^{-1} of integrated luminosity, collected by the LHCb experiment in 2010. A sample of $B^0 \rightarrow K^{*0} J/\psi$ ($J/\psi \rightarrow \mu^+ \mu^-$) candidates is used to represent the $B^0 \rightarrow K^{*0} \mu^+ \mu^-$ signal in the BDT training. Candidates from the $B^0 \rightarrow K^{*0} \mu^+ \mu^-$ upper mass sideband ($5350 < m(K^+ \pi^- \mu^+ \mu^-) < 5600 \text{ MeV}/c^2$) are used as a background sample. Candidates with invariant masses below the nominal B^0 mass contain a significant contribution from partially reconstructed B decays and are not used in the BDT training or in the subsequent analysis. They are removed by requiring that candidates have $m(K^+ \pi^- \mu^+ \mu^-) > 5150 \text{ MeV}/c^2$. The BDT uses predominantly geometric variables, including the variables used in the pre-selection (above). It also includes information on the quality of the B^0 vertex and the

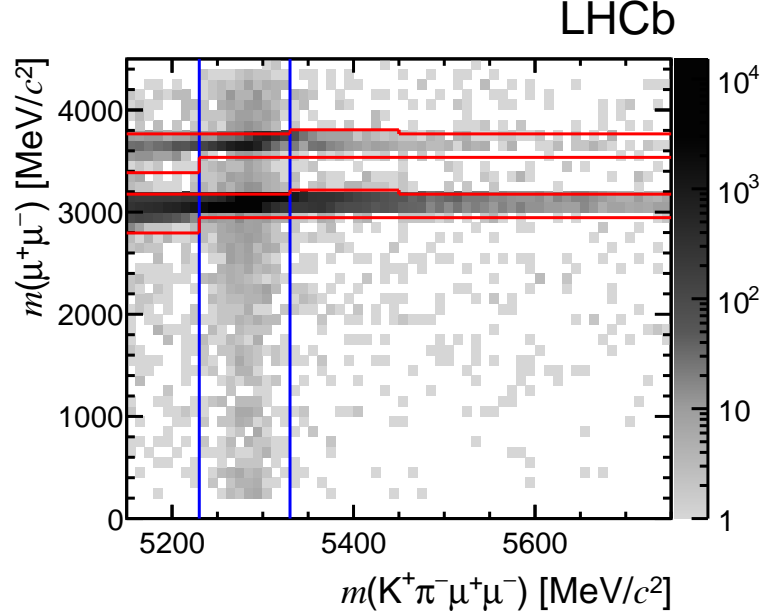


Figure 1: Distribution of $\mu^+\mu^-$ versus $K^+\pi^-\mu^+\mu^-$ invariant mass of selected $B^0 \rightarrow K^{*0}\mu^+\mu^-$ candidates. The vertical lines indicate a $\pm 50 \text{ MeV}/c^2$ signal mass window around the nominal B^0 mass. The horizontal lines indicate the two veto regions that are used to remove J/ψ and $\psi(2S) \rightarrow \mu^+\mu^-$ decays. The $B^0 \rightarrow K^{*0}\mu^+\mu^-$ signal is clearly visible outside of the J/ψ and $\psi(2S) \rightarrow \mu^+\mu^-$ windows.

fit χ^2 of the four tracks. Finally the BDT includes information from the RICH and muon systems on the likelihood that the kaon, pion and muons are correctly identified. Care has been taken, using simulated events, to ensure that the BDT does not preferentially select regions of q^2 , $K^+\pi^-\mu^+\mu^-$ invariant mass or of the $K^+\pi^-\mu^+\mu^-$ angular distribution. The multivariate selection removes 88% of the background that remains after the pre-selection and retains 78% of the signal.

Figure 1 shows the $\mu^+\mu^-$ versus $K^+\pi^-\mu^+\mu^-$ invariant mass of the selected candidates. The $B^0 \rightarrow K^{*0}\mu^+\mu^-$ signal, which peaks in $K^+\pi^-\mu^+\mu^-$ invariant mass, and populates the full range of the dimuon invariant mass range, is clearly visible.

4 Exclusive and partially reconstructed backgrounds

Several sources of peaking background have been studied using samples of simulated events, corrected to reflect the difference in particle identification (and misidentification) performance between the data and simulation. Sources of background that are not reduced to a negligible level by the pre- and multivariate-selections are described below.

The decays $B^0 \rightarrow K^{*0}J/\psi$ and $B^0 \rightarrow K^{*0}\psi(2S)$, where J/ψ and $\psi(2S) \rightarrow \mu^+\mu^-$, are removed by rejecting candidates with $2946 < m(\mu^+\mu^-) < 3176 \text{ MeV}/c^2$ and

122 $3586 < m(\mu^+\mu^-) < 3766 \text{ MeV}/c^2$. These vetoes are extended downwards by $150 \text{ MeV}/c^2$
123 in $m(\mu^+\mu^-)$ for $B^0 \rightarrow K^{*0}\mu^+\mu^-$ candidates with masses $5150 < m(K^+\pi^-\mu^+\mu^-) <$
124 $5230 \text{ MeV}/c^2$ to account for the radiative tails of the J/ψ and $\psi(2S)$ mesons. They are
125 also extended upwards by $25 \text{ MeV}/c^2$ for candidates with masses above the B^0 mass to
126 account for the small percentage of J/ψ or $\psi(2S)$ decays that are misreconstructed at
127 higher masses. The decay $B^0 \rightarrow K^{*0}J/\psi$ is used throughout this analysis as a control
128 channel. The J/ψ and $\psi(2S)$ vetoes are shown in Fig. 1.

129 The decay $B^0 \rightarrow K^{*0}J/\psi$ can also form a source of peaking background if the kaon or
130 pion is misidentified as a muon and swapped with one of the muons from the J/ψ decay.
131 This background is removed by rejecting candidates that have a $K^+\mu^-$ or $\pi^-\mu^+$ invariant
132 mass (where the kaon or pion is assigned the muon mass) in the range $3036 < m(\mu^+\mu^-) <$
133 $3156 \text{ MeV}/c^2$ if the kaon or pion can also be matched to hits in the muon stations. A
134 similar veto is applied for the decay $B^0 \rightarrow K^{*0}\psi(2S)$.

135 The decay $B_s^0 \rightarrow \phi\mu^+\mu^-$, where $\phi \rightarrow K^+K^-$, is removed by rejecting candidates if the
136 $K^+\pi^-$ mass is consistent with originating from a $\phi \rightarrow K^+K^-$ decay and the pion is kaon-like
137 according to the RICH detectors. A similar veto is applied to remove $\Lambda_b^0 \rightarrow \Lambda^*(1520)\mu^+\mu^-$
138 ($\Lambda^*(1520) \rightarrow pK^-$) decays.

139 There is also a source of background from the decay $B^+ \rightarrow K^+\mu^+\mu^-$ that appears
140 in the upper mass sideband and has a peaking structure in $\cos\theta_K$. This background
141 arises when a K^{*0} candidate is formed using a pion from the other B decay in the event
142 and is removed by vetoing events that have a $K^+\mu^+\mu^-$ invariant mass in the range
143 $5230 < m(K^+\mu^+\mu^-) < 5330 \text{ MeV}/c^2$. The fraction of combinatorial background candidates
144 removed by this veto is small.

145 After these selection requirements the dominant sources of peaking background are
146 expected to be from the decays $B^0 \rightarrow K^{*0}J/\psi$ (where the kaon or pion is misidentified
147 as a muon and a muon as a pion or kaon), $B_s^0 \rightarrow \phi\mu^+\mu^-$ and $\bar{B}_s^0 \rightarrow K^{*0}\mu^+\mu^-$ at the
148 levels of $(0.3 \pm 0.1)\%$, $(1.2 \pm 0.5)\%$ and $(1.0 \pm 1.0)\%$, respectively. The rate of the decay
149 $\bar{B}_s^0 \rightarrow K^{*0}\mu^+\mu^-$ is estimated using the fragmentation fraction f_s/f_d [21] and assuming the
150 branching fraction of this decay is suppressed by the ratio of CKM elements $|V_{td}/V_{ts}|^2$
151 with respect to $B^0 \rightarrow K^{*0}\mu^+\mu^-$. The full size of the effect is assigned as a systematic
152 uncertainty. Finally, the probability for a decay $B^0 \rightarrow K^{*0}\mu^+\mu^-$ to be misidentified as
153 $\bar{B}^0 \rightarrow \bar{K}^{*0}\mu^+\mu^-$ is estimated to be $(0.85 \pm 0.02)\%$ using simulated events.

154 5 Detector acceptance and selection biases

155 The geometrical acceptance of the detector, the trigger, the event reconstruction and
156 selection can all bias the angular distribution of the selected candidates. At low q^2 there
157 are large distortions of the angular distribution at extreme values of $\cos\theta_\ell$ ($|\cos\theta_\ell| \sim 1$).
158 These arise from the requirement that muons have momentum $p \gtrsim 3 \text{ GeV}/c$ to reach the
159 LHCb muon system. Distortions are also visible in the $\cos\theta_K$ angular distribution. They
160 arise from the momentum needed for a track to reach the tracking system downstream of
161 the dipole magnet, and from the impact parameter requirements made in the pre-selection.

The acceptance in $\cos\theta_K$ is asymmetric due to the momentum imbalance between the pion and kaon from the K^{*0} decay in the laboratory frame.

Acceptance effects are accounted for, in a model-independent way, in the angular and differential branching fraction analyses by weighting candidates by the inverse of their efficiency determined from simulation. This takes into account the variation of the acceptance in q^2 to give an unbiased estimate of the observables over the q^2 bin. The candidate weights are normalised such that they have mean 1.0. The resulting distribution of weights in each q^2 bin has a root-mean-square in the range 0.2 – 0.4. Only 2% of candidates have weights larger than 2.0.

The weights are determined using a large sample of simulated three-body $B^0 \rightarrow K^{*0}\mu^+\mu^-$ phase-space decays. They are determined separately in fine bins of q^2 with widths: $0.1 \text{ GeV}^2/c^4$ for $q^2 < 1 \text{ GeV}^2/c^4$; $0.2 \text{ GeV}^2/c^4$ in the range $1 < q^2 < 6 \text{ GeV}^2/c^4$; and $0.5 \text{ GeV}^2/c^4$ for $q^2 > 6 \text{ GeV}^2/c^4$. Inside the q^2 bins, the angular acceptance is assumed to factorise such that $\varepsilon(\cos\theta_\ell, \cos\theta_K, \phi) = \varepsilon(\cos\theta_\ell)\varepsilon(\cos\theta_K)\varepsilon(\phi)$. This factorisation is validated at the level of 5% in the phase-space sample. The treatment of the event weights is discussed in more detail in Sec. 7.

Event weights are also used to account for the fraction of background candidates that were removed in the lower mass ($m(K^+\pi^-\mu^+\mu^-) < 5230 \text{ MeV}/c^2$) and upper mass ($m(K^+\pi^-\mu^+\mu^-) > 5330 \text{ MeV}/c^2$) sidebands by the J/ψ and $\psi(2S)$ vetoes described in Sec. 4 (and shown in Fig. 1). In each q^2 bin, a linear extrapolation in q^2 is used to estimate this fraction and the resulting event weights. The weights are largest for the q^2 bin between the J/ψ and $\psi(2S)$ resonances.

6 Differential branching fraction

The angular and differential branching fraction analyses are performed in six bins of q^2 , which are the same as those used in Ref. [8]. The $K^+\pi^-\mu^+\mu^-$ invariant mass of candidates in these q^2 bins is shown in Fig. 2.

The number of signal candidates in each of the q^2 bins is estimated by performing an extended unbinned maximum likelihood fit to the $K^+\pi^-\mu^+\mu^-$ invariant mass distribution. The signal shape is taken from a fit to the $B^0 \rightarrow K^{*0}J/\psi$ control sample and is parameterised by the sum of two Crystal Ball [22] functions that differ only by the width of the Gaussian component. The combinatorial background is described by an exponential distribution. The decay $\bar{B}_s^0 \rightarrow K^{*0}\mu^+\mu^-$, which forms a peaking background, is assumed to have a shape identical to that of the $B^0 \rightarrow K^{*0}\mu^+\mu^-$ signal, but shifted in mass by the $B_s^0 - B^0$ mass difference [23]. Contributions from the decays $B_s^0 \rightarrow \phi\mu^+\mu^-$ and $B^0 \rightarrow K^{*0}J/\psi$ (where the μ^- is swapped with the π^-) are also included. The shapes of these backgrounds are taken from samples of simulated events. The sizes of the $\bar{B}_s^0 \rightarrow K^{*0}\mu^+\mu^-$, $B_s^0 \rightarrow \phi\mu^+\mu^-$ and $B^0 \rightarrow K^{*0}J/\psi$ backgrounds are fixed with respect to the $B^0 \rightarrow K^{*0}\mu^+\mu^-$ signal in the likelihood fit according to the ratios described in Sec. 4. These backgrounds are varied to evaluate the corresponding systematic uncertainty. The resulting signal yields are given in Table 1. In the full $0.1 < q^2 < 19.0 \text{ GeV}^2/c^4$ range, the fit yields 883 ± 34 signal decays.

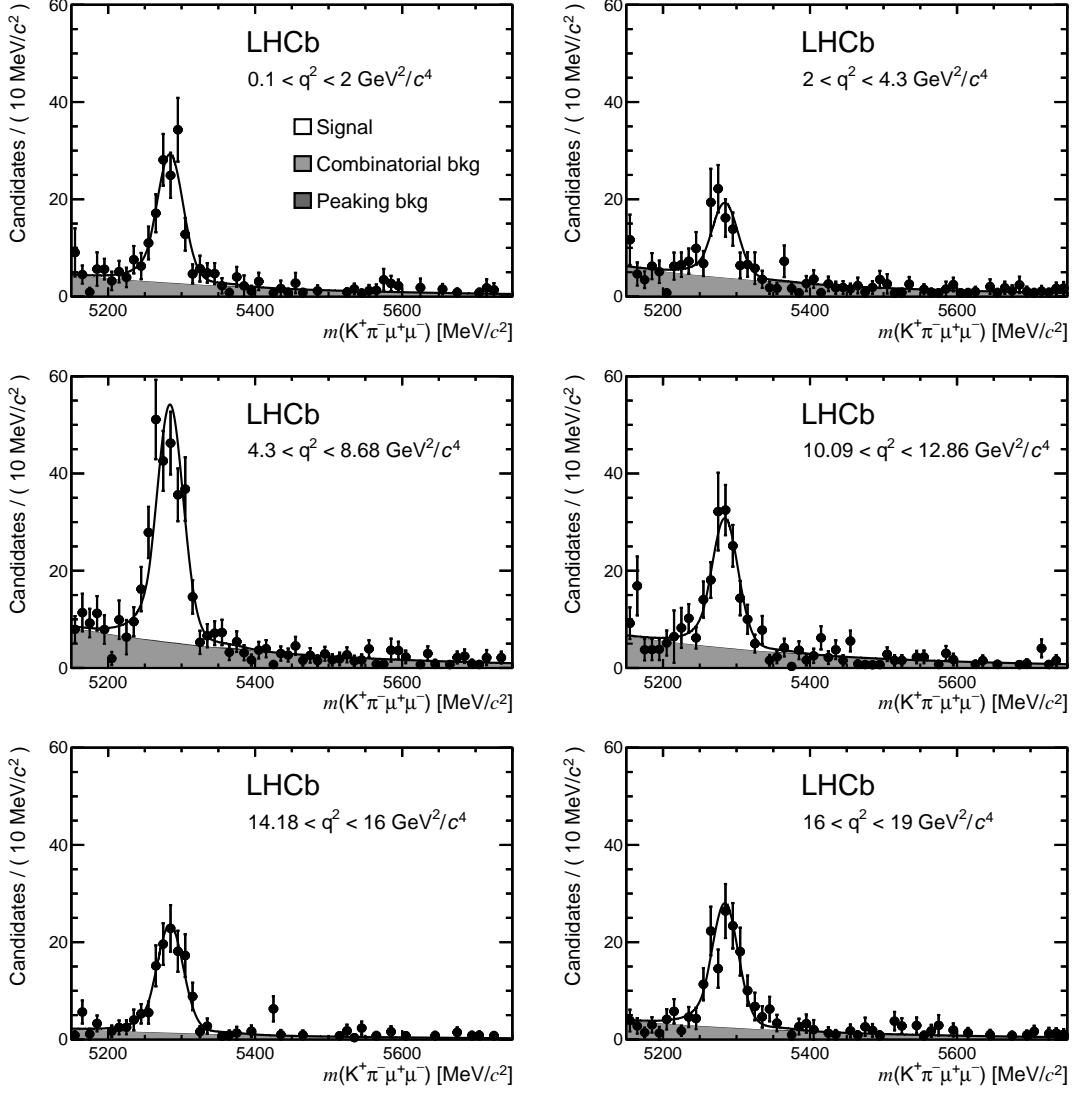


Figure 2: Invariant mass distributions of $K^+\pi^-\mu^+\mu^-$ candidates in the six q^2 bins used in the analysis. The candidates have been weighted to account for the detector acceptance (see text). Contributions from exclusive (peaking) backgrounds are negligible after applying the vetoes described in Sec. 4.

202 The differential branching fraction of the decay $B^0 \rightarrow K^{*0}\mu^+\mu^-$, in each q^2 bin, is
 203 estimated by normalising the $B^0 \rightarrow K^{*0}\mu^+\mu^-$ yield, N_{sig} , to the total event yield of the
 204 $B^0 \rightarrow K^{*0}J/\psi$ control sample, $N_{K^{*0}J/\psi}$, and correcting for the relative efficiency between
 205 the two decays, $\varepsilon_{K^{*0}J/\psi} / \varepsilon_{K^{*0}\mu^+\mu^-}$,

$$\frac{d\mathcal{B}}{dq^2} = \frac{1}{q_{\text{max}}^2 - q_{\text{min}}^2} \frac{N_{\text{sig}}}{N_{K^{*0}J/\psi}} \frac{\varepsilon_{K^{*0}J/\psi}}{\varepsilon_{K^{*0}\mu^+\mu^-}} \times \mathcal{B}(B^0 \rightarrow K^{*0}J/\psi) \times \mathcal{B}(J/\psi \rightarrow \mu^+\mu^-). \quad (3)$$

Table 1: Signal yield (N_{sig}) and differential branching fraction ($d\mathcal{B}/dq^2$) of the $B^0 \rightarrow K^{*0} \mu^+ \mu^-$ decay in the six q^2 bins used in this analysis. Results are also presented in the $1 < q^2 < 6 \text{ GeV}^2/c^4$ range where theoretical uncertainties are best controlled. The first and second uncertainties are statistical and systematic. The third uncertainty comes from the uncertainty on the $B^0 \rightarrow K^{*0} J/\psi$ and $J/\psi \rightarrow \mu^+ \mu^-$ branching fractions. The final uncertainty on $d\mathcal{B}/dq^2$ comes from an estimate of the pollution from non- $K^{*0} B^0 \rightarrow K^+ \pi^- \mu^+ \mu^-$ decays in the $792 < m(K^+ \pi^-) < 992 \text{ MeV}/c^2$ mass window (see Sec. 7.3.1).

q^2 (GeV^2/c^4)	N_{sig}	$d\mathcal{B}/dq^2$ ($10^{-7} \text{ GeV}^{-2} c^4$)
0.10 – 2.00	140 ± 13	$0.60 \pm 0.06 \pm 0.05 \pm 0.04^{+0.00}_{-0.05}$
2.00 – 4.30	73 ± 11	$0.30 \pm 0.03 \pm 0.03 \pm 0.02^{+0.00}_{-0.02}$
4.30 – 8.68	271 ± 19	$0.49 \pm 0.04 \pm 0.04 \pm 0.03^{+0.00}_{-0.04}$
10.09 – 12.86	168 ± 15	$0.43 \pm 0.04 \pm 0.04 \pm 0.03^{+0.00}_{-0.03}$
14.18 – 16.00	115 ± 12	$0.56 \pm 0.06 \pm 0.04 \pm 0.04^{+0.00}_{-0.05}$
16.00 – 19.00	116 ± 13	$0.41 \pm 0.04 \pm 0.04 \pm 0.03^{+0.00}_{-0.03}$
1.00 – 6.00	197 ± 17	$0.34 \pm 0.03 \pm 0.04 \pm 0.02^{+0.00}_{-0.03}$

206 The branching fractions $\mathcal{B}(B^0 \rightarrow K^{*0} J/\psi)$ and $\mathcal{B}(J/\psi \rightarrow \mu^+ \mu^-)$ are $(1.31 \pm 0.03 \pm 0.08) \times$
207 10^{-3} [24] and $(5.93 \pm 0.06) \times 10^{-2}$ [23], respectively.

208 The efficiency ratio, $\varepsilon_{K^{*0} J/\psi} / \varepsilon_{K^{*0} \mu^+ \mu^-}$, depends on the unknown angular distribution of
209 the $B^0 \rightarrow K^{*0} \mu^+ \mu^-$ decay. To avoid making any assumption on the angular distribution,
210 the event-by-event weights described in Sec. 5 are used to estimate the average efficiency
211 of the $B^0 \rightarrow K^{*0} J/\psi$ candidates and the signal candidates in each q^2 bin.

212 The resulting differential branching fraction of the decay $B^0 \rightarrow K^{*0} \mu^+ \mu^-$ is shown in
213 Fig. 3 and in Table 1. The bands shown in Fig. 3 indicate the theoretical prediction for
214 the differential branching fraction. The calculation of the bands is described in Ref. [25].²
215 In the low q^2 region, the calculations are based on QCD factorisation and soft collinear
216 effective theory (SCET) [27], which profit from having a heavy B^0 meson and an energetic
217 K^{*0} meson. In the soft-recoil, high q^2 region, an operator product expansion (OPE) in
218 inverse b -quark mass ($1/m_b$) and $1/\sqrt{q^2}$ is used to estimate the long-distance contributions
219 from quark loops [28, 29]. No theory prediction is included in the region close to the
220 narrow $c\bar{c}$ resonances (the J/ψ and $\psi(2S)$) where the assumptions from QCD factorisation,
221 SCET and the OPE break down. The form-factor calculations are taken from Ref. [30].
222 A dimensional estimate is made of the uncertainty on the decay amplitudes from QCD
223 factorisation and SCET of $\mathcal{O}(\Lambda_{\text{QCD}}/m_b)$ [31]. Contributions from light-quark resonances
224 at large recoil (low q^2) have been neglected. A discussion of these contributions can be
225 found in Ref. [32].

²A consistent set of SM predictions, averaged over each q^2 bin, have recently also been provided by the authors of Ref. [26].

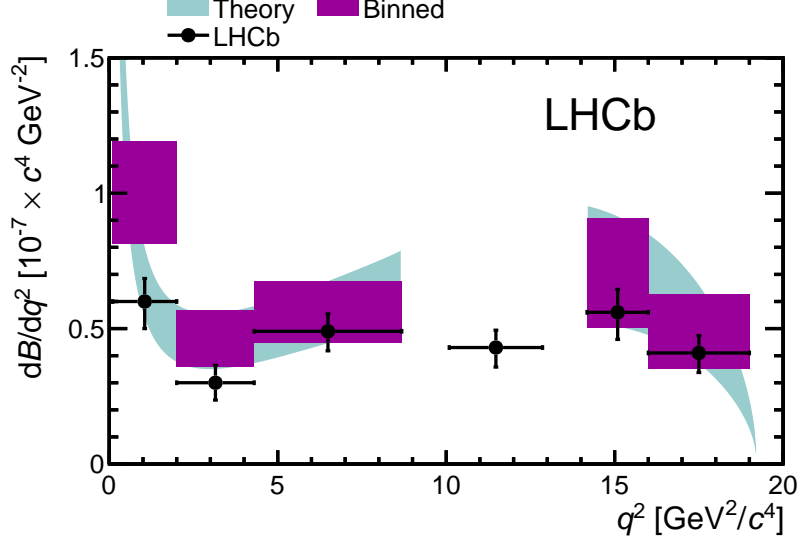


Figure 3: Differential branching fraction of the $B^0 \rightarrow K^{*0} \mu^+ \mu^-$ decay as a function of the dimuon invariant mass squared. The data are overlaid with a SM prediction (see text) for the decay (light-blue band). A rate average of the SM prediction across each q^2 bin is indicated by the dark (purple) rectangular regions. No SM prediction is included in the region close to the narrow $c\bar{c}$ resonances.

6.1 Systematic uncertainties on the differential branching fraction

The largest sources of systematic uncertainty on the differential branching fraction come from the $\sim 6\%$ uncertainty on the combined $B^0 \rightarrow K^{*0} J/\psi$ and $J/\psi \rightarrow \mu^+ \mu^-$ branching fractions and from the uncertainty on the pollution of non- K^{*0} decays in the $792 < m(K^+ \pi^-) < 992 \text{ MeV}/c^2$ mass window (see Sec. 7.3.1). No S-wave correction needs to be applied to the observed yield of $B^0 \rightarrow K^{*0} J/\psi$ decays because the branching fraction used in the normalisation (from Ref. [24]) corresponds to a measurement of the decay $B^0 \rightarrow K^+ \pi^- J/\psi$ over the same mass window used in this analysis.

The uncertainty associated with the corrections used to calibrate the performance of the simulation is $1 - 2\%$. Varying the level of the peaking backgrounds within their uncertainties changes the differential branching fraction by 1% . In the simulation a small variation in the $K^+ \pi^- \mu^+ \mu^-$ invariant mass resolution is seen between $B^0 \rightarrow K^{*0} J/\psi$ and $B^0 \rightarrow K^{*0} \mu^+ \mu^-$ decays at low or high q^2 . Conservatively, the width of the signal mass model is varied by up to 5% in every q^2 bin and the deviation from the nominal fit is assigned as a systematic uncertainty.

7 Angular analysis

The $B^0 \rightarrow K^{*0} \mu^+ \mu^-$ angular distribution is reduced to

$$\begin{aligned} \frac{1}{d\Gamma/dq^2} \frac{d^4\Gamma}{dq^2 d\cos\theta_\ell d\cos\theta_K d\hat{\phi}} = \frac{9}{16\pi} \bigg[& F_L \cos^2\theta_K + \frac{3}{4}(1 - F_L)(1 - \cos^2\theta_K) - \\ & F_L \cos^2\theta_K(2\cos^2\theta_\ell - 1) + \\ & \frac{1}{4}(1 - F_L)(1 - \cos^2\theta_K)(2\cos^2\theta_\ell - 1) + \\ & S_3(1 - \cos^2\theta_K)(1 - \cos^2\theta_\ell) \cos 2\hat{\phi} + \\ & \frac{4}{3}A_{\text{FB}}(1 - \cos^2\theta_K) \cos\theta_\ell + \\ & A_9(1 - \cos^2\theta_K)(1 - \cos^2\theta_\ell) \sin 2\hat{\phi} \bigg] \end{aligned} \quad (4)$$

after requiring that $q^2 \gg 4m_\mu^2$ and applying the transformation from $\phi \rightarrow \hat{\phi}$ described by Eq. 2. The parameters A_{FB} , F_L , S_3 and A_9 must satisfy the constraints

$$|A_{\text{FB}}| \leq \frac{3}{4}(1 - F_L), \quad |A_9| \leq \frac{1}{2}(1 - F_L) \quad \text{and} \quad |S_3| \leq \frac{1}{2}(1 - F_L)$$

for Eq. 4 to remain positive in all regions of the allowed phase space. These relationships are automatically taken into account in the transformations

$$A_{\text{FB}} = \frac{3}{4}(1 - F_L)A_{\text{T}}^{\text{Re}} \quad \text{and} \quad S_3 = \frac{1}{2}(1 - F_L)A_{\text{T}}^2,$$

which map A_{FB} and S_3 to the theoretically cleaner transverse observables, A_{T}^{Re} and A_{T}^2 . There are less trivial relationships between S_3 , A_9 and A_{FB} , which all depend on the same underlying decay amplitudes (see for example Ref. [33]). These relationships are not reproduced here.

In each of the q^2 bins, A_{FB} (A_{T}^{Re}), F_L , S_3 (A_{T}^2) and A_9 are estimated by performing an unbinned maximum likelihood fit to the $\cos\theta_\ell$, $\cos\theta_K$ and $\hat{\phi}$ distributions of the $B^0 \rightarrow K^{*0} \mu^+ \mu^-$ candidates. The $K^+ \pi^- \mu^+ \mu^-$ invariant mass of the candidates is also included in the fit to separate between signal- and background-like candidates. The background angular distribution is described using the product of three second-order Chebychev polynomials under the assumption that the background can be factorised into three single angle distributions. This assumption has been validated on the data sidebands ($5350 < m(K^+ \pi^- \mu^+ \mu^-) < 5600 \text{ MeV}/c^2$). A dilution factor ($\mathcal{D} = 1 - 2\omega$) is included in the likelihood fit for A_{FB} and A_9 , to account at first order for the small probability (ω) for a decay $\bar{B}^0 \rightarrow \bar{K}^{*0} \mu^+ \mu^-$ to be misidentified as $B^0 \rightarrow K^{*0} \mu^+ \mu^-$. The value of ω is fixed to 0.85% in the fit (see Sec. 4).

Two fits to the dataset are performed: one, with the signal angular distribution described by Eq. 4, to measure F_L , A_{FB} , S_3 and A_9 and a second replacing A_{FB} and S_3

with the observables A_T^{Re} and A_T^2 . The angular observables vary with q^2 within the q^2 bins used in the analysis. The measured quantities therefore correspond to averages over these q^2 bins. For the transverse observables, where the observable appears alongside $1 - F_L$ in the angular distribution, the averaging is complicated by the q^2 dependence of both the observable and F_L . In this case, the measured quantity corresponds to a weighted average of the transverse observable over q^2 , with a weight $(1 - F_L)d\Gamma/dq^2$.

7.1 Statistical uncertainty on the angular observables

The results of the angular fits are presented in Table 2 and in Figs. 4 and 5. The 68% confidence intervals are estimated using pseudo-experiments and the Feldman-Cousins technique [34].³ This avoids any potential bias on the parameter uncertainty that could have otherwise come from using event weights in the likelihood fit or from boundary issues arising in the fitting. The observables are each treated separately in this procedure. For example, when determining the interval on A_{FB} , the observables F_L , S_3 and A_9 are treated as if they were nuisance parameters. At each value of the angular observable being considered, the maximum likelihood estimate of the nuisance parameters (which also include the background parameters) is used when generating the pseudo-experiments. The resulting confidence intervals do not express correlations between the different observables. The treatment of systematic uncertainties on the angular observables is described in Sec. 7.3.

The final column of Table 2 contains the p-value of the SM point in each q^2 bin, which is defined as the probability to observe a difference between the log-likelihood of the SM point compared to the best fit point larger than that seen in the data. They are estimated in a similar way to the Feldman-Cousins intervals by: generating a large ensemble of pseudo-experiments, with all of the angular observables fixed to the central value of the SM prediction; and performing two fits to the pseudo-experiments, one with all of the angular observables fixed to their SM values and one varying them freely. The data are then fitted in a similar manner and the p-value estimated by comparing the ratio of likelihoods obtained for the data to those of the pseudo-experiments. The p-values lie in the range 0.18 – 0.72 and indicate good agreement with the SM hypothesis.

As a cross-check, a third fit is also performed in which the sign of the angle ϕ for \bar{B}^0 decays is flipped to measure S_9 in place of A_9 in the angular distribution. The term S_9 is expected to be suppressed by the size of the strong phases and be close to zero in every q^2 bin. A_{FB} has also been cross-checked by performing a counting experiment in bins of q^2 . A consistent result is obtained in every bin.

³Nuisance parameters are treated according to the “plug-in” method (see, for example, Ref. [35]).

Table 2: Fraction of longitudinal polarisation of the K^{*0} , F_L , dimuon system forward-backward asymmetry, A_{FB} and the angular observables S_3 , S_9 and A_9 from the $B^0 \rightarrow K^{*0} \mu^+ \mu^-$ decay in the six bins of dimuon invariant mass squared, q^2 , used in the analysis. The lower table includes the transverse observables A_T^{Re} and A_T^2 , which have reduced form-factor uncertainties. Results are also presented in the $1 < q^2 < 6 \text{ GeV}^2/c^4$ range where theoretical uncertainties are best controlled. In the large-recoil bin, $0.1 < q^2 < 2.0 \text{ GeV}^2/c^4$, two results are given to highlight the size of the correction needed to account for changes in the angular distribution that occur when $q^2 \lesssim 1 \text{ GeV}^2/c^4$ (see Sec. 7.2). The final column contains the p-value for the SM point (see text). No SM prediction, and consequently no p-value, is available for the $10.09 < q^2 < 12.86 \text{ GeV}^2/c^4$ range.

q^2 (GeV^2/c^4)	F_L	A_{FB}	S_3	S_9
0.10 – 2.00 (uncorrected)	$0.37^{+0.10}_{-0.09}^{+0.04}_{-0.03}$	$-0.02^{+0.12}_{-0.12}^{+0.01}_{-0.01}$	$-0.04^{+0.10}_{-0.10}^{+0.01}_{-0.01}$	$0.05^{+0.10}_{-0.09}^{+0.01}_{-0.01}$
0.10 – 2.00 (corrected)	$0.37^{+0.10}_{-0.09}^{+0.04}_{-0.03}$	$-0.02^{+0.13}_{-0.13}^{+0.01}_{-0.01}$	$-0.05^{+0.12}_{-0.12}^{+0.01}_{-0.01}$	$0.06^{+0.12}_{-0.12}^{+0.01}_{-0.01}$
2.00 – 4.30	$0.74^{+0.10}_{-0.09}^{+0.02}_{-0.03}$	$-0.20^{+0.08}_{-0.08}^{+0.01}_{-0.01}$	$-0.04^{+0.10}_{-0.06}^{+0.01}_{-0.01}$	$-0.03^{+0.11}_{-0.04}^{+0.01}_{-0.01}$
4.30 – 8.68	$0.57^{+0.07}_{-0.07}^{+0.03}_{-0.03}$	$0.16^{+0.06}_{-0.05}^{+0.01}_{-0.01}$	$0.08^{+0.07}_{-0.06}^{+0.01}_{-0.01}$	$0.01^{+0.07}_{-0.08}^{+0.01}_{-0.01}$
10.09 – 12.86	$0.48^{+0.08}_{-0.09}^{+0.03}_{-0.03}$	$0.28^{+0.07}_{-0.06}^{+0.02}_{-0.02}$	$-0.16^{+0.11}_{-0.07}^{+0.01}_{-0.01}$	$-0.01^{+0.10}_{-0.11}^{+0.01}_{-0.01}$
14.18 – 16.00	$0.33^{+0.08}_{-0.07}^{+0.02}_{-0.03}$	$0.51^{+0.07}_{-0.05}^{+0.02}_{-0.02}$	$0.03^{+0.09}_{-0.10}^{+0.01}_{-0.01}$	$0.00^{+0.09}_{-0.08}^{+0.01}_{-0.01}$
16.00 – 19.00	$0.38^{+0.09}_{-0.07}^{+0.03}_{-0.03}$	$0.30^{+0.08}_{-0.08}^{+0.01}_{-0.02}$	$-0.22^{+0.10}_{-0.09}^{+0.02}_{-0.01}$	$0.06^{+0.11}_{-0.10}^{+0.01}_{-0.01}$
1.00 – 6.00	$0.65^{+0.08}_{-0.07}^{+0.03}_{-0.03}$	$-0.17^{+0.06}_{-0.06}^{+0.01}_{-0.01}$	$0.03^{+0.07}_{-0.07}^{+0.01}_{-0.01}$	$0.07^{+0.09}_{-0.08}^{+0.01}_{-0.01}$

q^2 (GeV^2/c^4)	A_9	A_T^2	A_T^{Re}	p-value
0.10 – 2.00 (uncorrected)	$0.12^{+0.09}_{-0.09}^{+0.01}_{-0.01}$	$-0.14^{+0.34}_{-0.30}^{+0.02}_{-0.02}$	$-0.04^{+0.26}_{-0.24}^{+0.02}_{-0.01}$	0.18
0.10 – 2.00 (corrected)	$0.14^{+0.11}_{-0.11}^{+0.01}_{-0.01}$	$-0.19^{+0.40}_{-0.35}^{+0.02}_{-0.02}$	$-0.06^{+0.29}_{-0.27}^{+0.02}_{-0.01}$	—
2.00 – 4.30	$0.06^{+0.12}_{-0.08}^{+0.01}_{-0.01}$	$-0.29^{+0.65}_{-0.46}^{+0.02}_{-0.03}$	$-1.00^{+0.13}_{-0.00}^{+0.04}_{-0.00}$	0.57
4.30 – 8.68	$-0.13^{+0.07}_{-0.07}^{+0.01}_{-0.01}$	$0.36^{+0.30}_{-0.31}^{+0.03}_{-0.03}$	$0.50^{+0.16}_{-0.14}^{+0.01}_{-0.03}$	0.71
10.09 – 12.86	$0.00^{+0.11}_{-0.11}^{+0.01}_{-0.01}$	$-0.60^{+0.42}_{-0.27}^{+0.05}_{-0.02}$	$0.71^{+0.15}_{-0.15}^{+0.01}_{-0.03}$	—
14.18 – 16.00	$-0.06^{+0.11}_{-0.08}^{+0.01}_{-0.01}$	$0.07^{+0.26}_{-0.28}^{+0.02}_{-0.02}$	$1.00^{+0.00}_{-0.05}^{+0.00}_{-0.02}$	0.38
16.00 – 19.00	$0.00^{+0.11}_{-0.10}^{+0.01}_{-0.01}$	$-0.71^{+0.35}_{-0.26}^{+0.06}_{-0.04}$	$0.64^{+0.15}_{-0.15}^{+0.01}_{-0.02}$	0.28
1.00 – 6.00	$0.03^{+0.08}_{-0.08}^{+0.01}_{-0.01}$	$0.15^{+0.39}_{-0.41}^{+0.03}_{-0.03}$	$-0.66^{+0.24}_{-0.22}^{+0.04}_{-0.01}$	0.72

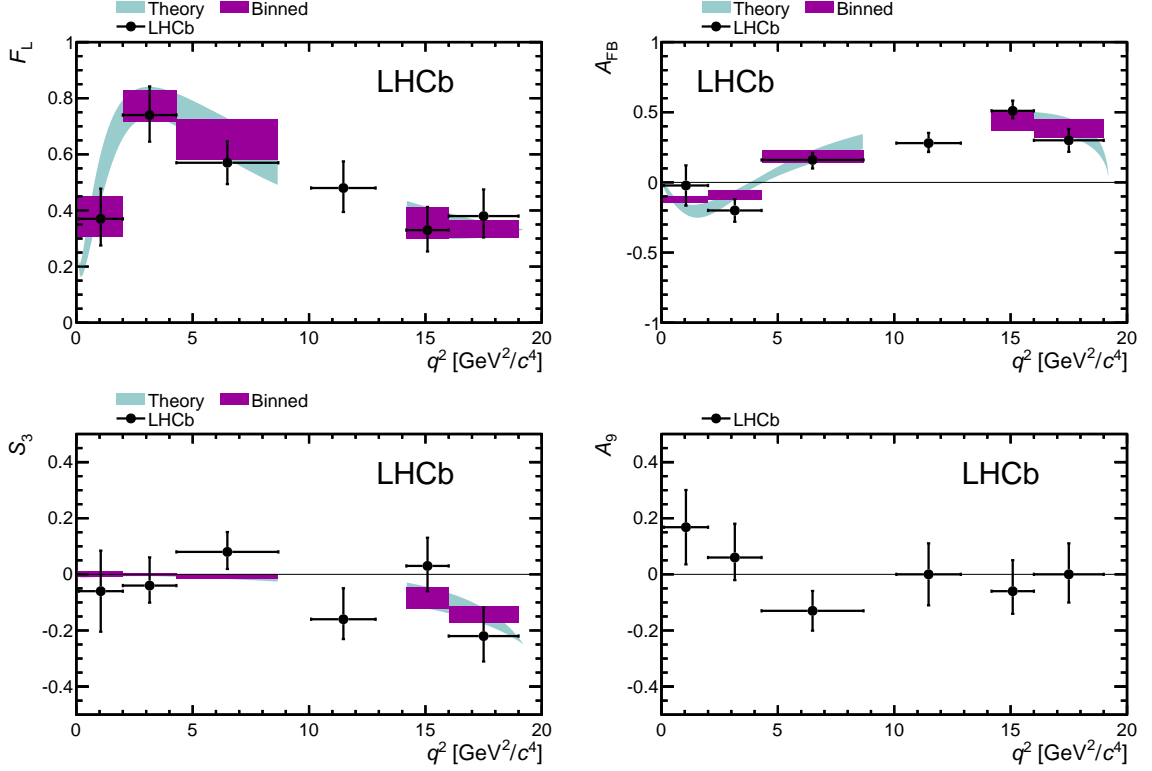


Figure 4: Fraction of longitudinal polarisation of the K^{*0} , F_L , dimuon system forward-backward asymmetry, A_{FB} and the angular observables S_3 and A_9 from the $B^0 \rightarrow K^{*0} \mu^+ \mu^-$ decay as a function of the dimuon invariant mass squared, q^2 . The lowest q^2 bin has been corrected for the threshold behaviour described in Sec. 7.2. The experimental data points overlay the SM prediction described in the text. A rate average of the SM prediction across each q^2 bin is indicated by the dark (purple) rectangular regions. No theory prediction is included for A_9 , which is vanishingly small in the SM.

7.2 Angular distribution at large recoil

Equation 4 assumes that $q^2 \gg 4m_\mu^2$, where m_μ is the muon mass. This assumption is valid for $q^2 \gtrsim 1 \text{ GeV}^2/c^4$ but breaks down in the largest recoil, lowest q^2 bin. In the $0.1 < q^2 < 2.0 \text{ GeV}^2/c^4$ range, the angular terms contain an additional q^2 dependence [1], proportional to

$$\frac{1 - 4m_\mu^2/q^2}{1 + 2m_\mu^2/q^2} \quad \text{or} \quad \frac{(1 - 4m_\mu^2/q^2)^{1/2}}{1 + 2m_\mu^2/q^2} \quad (5)$$

depending on the angular term.

As q^2 tends to zero, these threshold terms dilute the influence of the observables on the angular distribution. This dilution leads to a discrepancy between the experimental definition of the observables, where this additional q^2 dependence is neglected, and the

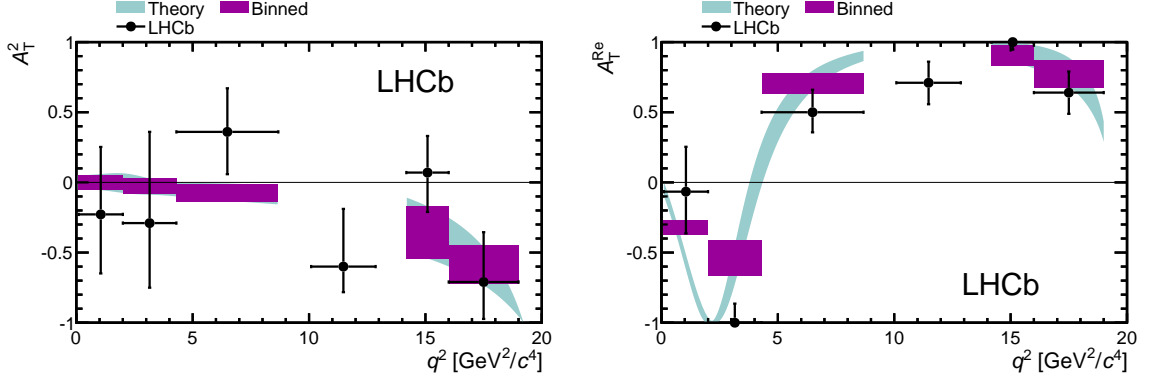


Figure 5: Transverse asymmetries A_T^2 and A_T^{Re} as a function of the dimuon invariant mass squared, q^2 , in the $B^0 \rightarrow K^{*0} \mu^+ \mu^-$ decay. The lowest q^2 bin has been corrected for the threshold behaviour described in Sec. 7.2. The experimental data points overlay the SM prediction that is described in the text. A rate average of the SM prediction across each q^2 bin is indicated by the dark (purple) rectangular regions.

definition of the observables in terms of the K^{*0} transversity amplitudes. The fraction of longitudinal polarisation of the K^{*0} meson, F_L , is the only observable that is unaffected by the additional terms; sensitivity to F_L arises mainly through the shape of the $\cos \theta_K$ distribution and this shape remains the same whether the threshold terms are included or not.

In order to estimate the size of the dilution, it is assumed that A_9 and A_T^2 are constant over the $0.1 < q^2 < 2 \text{ GeV}^2/c^4$ region and A_T^{Re} rises linearly (with the constraint that $A_T^{\text{Re}} = 0$ at $q^2 = 0$). The dilution of S_3 (A_{FB}) is derived from the relationship between the observable and A_T^2 (A_T^{Re}). Even though F_L is in itself unbiased, an assumption needs to be made about the q^2 dependence of F_L when determining the dilution of the other observables. An empirical model,

$$F_L(q^2) = \frac{aq^2}{1 + aq^2} \quad , \quad (6)$$

is used. This functional form displays the correct behaviour since it tends to zero as $q^2 \rightarrow 0$ and rises slowly over the q^2 bin. The coefficient $a = 0.67^{+0.54}_{-0.30}$ is estimated from the average of F_L obtained from the fit to the $0.1 < q^2 < 2.0 \text{ GeV}^2/c^4$ bin.

To remain model independent, the dilution factors are estimated by summing over the (background subtracted) signal candidates in the $0.1 < q^2 < 2 \text{ GeV}^2/c^4$ region. An example of how this is performed is given in Appendix B for the observable A_T^2 . The typical size of the correction is 10 – 20%. The values of the angular observables, after correcting for the dilution, are included in Table 2. A similar factor is also applied to the statistical uncertainty on the fit parameters to scale them accordingly. No systematic uncertainty is assigned to this correction.

The procedure to calculate the dilution factors has been validated using large samples

of simulated events, generated according to the SM prediction and several other scenarios in which large deviations from the SM expectation of the angular observables are possible. In all cases an unbiased estimate of the angular observables is obtained after applying the correction procedure. Different hypotheses for the q^2 dependence of F_L , A_{FB} and A_{T}^{Re} do not give large variations in the size of the correction factors.

7.3 Systematic uncertainties in the angular analysis

Sources of systematic uncertainty are considered if they introduce either an angular or q^2 dependent bias to the acceptance correction. Moreover, three assumptions have been made that may affect the interpretation of the result of the fit to the $K^+\pi^-\mu^+\mu^-$ invariant mass or angular distribution: that $q^2 \gg 4m_\mu^2$; that there are equal numbers of B^0 and \bar{B}^0 decays; and that there is no contribution from non- K^{*0} $B^0 \rightarrow K^+\pi^-\mu^+\mu^-$ decays in the $792 < m(K^+\pi^-) < 992 \text{ MeV}/c^2$ mass window. The first assumption was addressed in Sec. 7.2 and no systematic uncertainty is assigned to this correction. The number of B^0 and \bar{B}^0 candidates in the data set is very similar [36]. The resulting systematic uncertainty is addressed in Sec. 7.3.2. The final assumption is discussed in Sec. 7.3.1 below.

The full fitting procedure has been tested on $B^0 \rightarrow K^{*0}J/\psi$ decays. In this larger data sample, A_{FB} is found to be consistent with zero (as expected) and the other observables are in agreement with the results of Ref. [37]. There is however a small discrepancy between the expected parabolic shape of the $\cos\theta_K$ distribution and the distribution of the $B^0 \rightarrow K^{*0}J/\psi$ candidates after weighting the candidates to correct for the detector acceptance. This percent-level discrepancy could point to a bias in the acceptance model. To account for this discrepancy, and any breakdown in the assumption that the efficiencies in $\cos\theta_\ell$, $\cos\theta_K$ and ϕ are independent, systematic variations of the weights are tried in which they are conservatively rescaled by 10% at the edges of $\cos\theta_\ell$, $\cos\theta_K$ and ϕ with respect to the centre. Several possible variations are explored, including variations that are non-factorisable. The variation which has the largest effect on each of the angular observables is assigned as a systematic uncertainty. The resulting systematic uncertainties are at the level of 0.01 – 0.03 and are largest for the transverse observables.

The uncertainties on the signal mass model have little effect on the angular observables. Of more importance are potential sources of uncertainty on the background shape. In the angular fit the background is modelled as the product of three second-order polynomials, the parameters of which are allowed to vary freely in the likelihood fit. This model describes the data well in the sidebands. As a cross-check, alternative fits are performed both using higher order polynomials and by fixing the shape of the background to be flat in $\cos\theta_\ell$, $\cos\theta_K$ and $\hat{\phi}$. The largest shifts in the angular observables occur for the flat background model and are at the level of 0.01 – 0.06 and 0.02 – 0.25 for the transverse observables (they are at most 65% of the statistical uncertainty). These variations are extreme modifications of the background model and are not considered further as sources of systematic uncertainty.

The angular distributions of the decays $B_s^0 \rightarrow \phi\mu^+\mu^-$ and $\bar{B}_s^0 \rightarrow K^{*0}\mu^+\mu^-$ are both poorly known. The decay $\bar{B}_s^0 \rightarrow K^{*0}\mu^+\mu^-$ is yet to be observed. A first measurement of

Table 3: Systematic contributions to the angular observables. The values given are the magnitude of the maximum contribution from each source of systematic uncertainty, taken across the six principal q^2 bins used in the analysis.

Source	A_{FB}	F_L	S_3	S_9	A_9	A_{T}^2	A_{T}^{Re}
Acceptance model	0.02	0.03	0.01	< 0.01	< 0.01	0.02	0.01
Mass model	< 0.01	< 0.01	< 0.01	< 0.01	< 0.01	< 0.01	< 0.01
$B^0 \rightarrow \bar{B}^0$ mis-id	< 0.01	< 0.01	< 0.01	< 0.01	0.01	< 0.01	< 0.01
Data-simulation diff.	0.01	0.03	0.01	< 0.01	< 0.01	0.03	0.01
Kinematic reweighting	< 0.01	0.01	< 0.01	< 0.01	< 0.01	0.01	< 0.01
Peaking backgrounds	0.01	0.01	0.01	0.01	0.01	0.01	0.01
S-wave	0.01	0.01	0.02	0.01	< 0.01	0.05	0.04
B^0 - \bar{B}^0 asymmetries	< 0.01	< 0.01	< 0.01	< 0.01	< 0.01	< 0.01	< 0.01

$B_s^0 \rightarrow \phi \mu^+ \mu^-$ has been made in Ref. [38]. In the likelihood fit to the angular distribution these backgrounds are neglected. A conservative systematic uncertainty on the angular observables is assigned at the level of $\lesssim 0.01$ by assuming that the peaking backgrounds have an identical shape to the signal, but have an angular distribution in which each of the observables is either maximal or minimal.

Systematic variations are also considered for the data-derived corrections to the simulated events. For example, the muon identification efficiency, which is derived from data using a tag-and-probe approach with J/ψ decays, is varied within its uncertainty in opposite direction for high ($p > 10 \text{ GeV}/c$) and low ($p < 10 \text{ GeV}/c$) momentum muons. Similar variations are applied to the other data-derived corrections, yielding a combined systematic uncertainty at the level of $0.01 - 0.02$ on the angular observables. The correction needed to account for differences between data and simulation in the B^0 momentum spectrum is small. If this correction is neglected, the angular observables vary by at most 0.01 . This variation is associated as a systematic uncertainty.

The systematic uncertainties arising from the variations of the angular acceptance are assessed using pseudo-experiments that are generated with one acceptance model and fitted according to a different model. Consistent results are achieved by varying the event weights applied to the data and repeating the likelihood fit.

A summary of the different contributions to the total systematic uncertainty can be found in Table 3. The systematic uncertainty on the angular observables in Table 2 is the result of adding these contributions in quadrature.

7.3.1 Influence of S-wave interference on the angular distribution

The presence of a non- K^{*0} $B^0 \rightarrow K^+ \pi^- \mu^+ \mu^-$ component, where the $K^+ \pi^-$ system is in an S-wave configuration, modifies Eq. 4 to

$$\frac{1}{d\Gamma'/dq^2} \frac{d^4\Gamma'}{dq^2 d\cos\theta_\ell d\cos\theta_K d\hat{\phi}} = (1 - F_S) \left[\frac{1}{d\Gamma/dq^2} \frac{d^4\Gamma}{dq^2 d\cos\theta_\ell d\cos\theta_K d\hat{\phi}} \right] + \frac{9}{16\pi} \left[\frac{2}{3} F_S (1 - \cos^2\theta_\ell) + \frac{4}{3} A_S \cos\theta_K (1 - \cos^2\theta_\ell) \right], \quad (7)$$

where F_S is the fraction of $B^0 \rightarrow K^+ \pi^- \mu^+ \mu^-$ S-wave in the $792 < m(K^+ \pi^-) < 992 \text{ MeV}/c^2$ window. The partial width, Γ' , is the sum of the partial widths for the $B^0 \rightarrow K^{*0} \mu^+ \mu^-$ decay and the $B^0 \rightarrow K^+ \pi^- \mu^+ \mu^-$ S-wave. A forward-backward asymmetry in $\cos\theta_K$, A_S , arises due to the interference between the longitudinal amplitude of the K^{*0} and the S-wave amplitude [39–42].

The S-wave is neglected in the results given in Table 2. To estimate the size of the S-wave component, and the impact it might have on the $B^0 \rightarrow K^{*0} \mu^+ \mu^-$ angular analysis, the phase shift of the K^{*0} Breit-Wigner function around the K^{*0} pole mass is exploited. Instead of measuring F_S directly, the average value of A_S is measured in two bins of $K^+ \pi^-$ invariant mass, one below and one above the K^{*0} pole mass. If the magnitude and phase of the S-wave amplitude are assumed to be independent of the $K^+ \pi^-$ invariant mass in the range $792 < m(K^+ \pi^-) < 992 \text{ MeV}/c^2$, and the P-wave amplitude is modelled by a Breit-Wigner function, the two A_S values can then be used to determine the real and imaginary components of the S-wave amplitude (and F_S).⁴

For a small S-wave amplitude, the pure S-wave contribution, F_S , to Eq. 7 has only a small effect on the angular distribution. The magnitude of A_S arising from the interference between the S- and P-wave can however still be sizable and this information is exploited by this phase-shift method. The method, described above, is statistically more precise than fitting Eq. 7 directly for A_S and F_S as uncorrelated variables. For the $B^0 \rightarrow K^{*0} J/\psi$ control mode, the gain in statistical precision is approximately a factor of three.

Due to the limited number of signal candidates that are available in each of the q^2 bins, the bins are merged in order to estimate the S-wave fraction. In the range $0.1 < q^2 < 19 \text{ GeV}^2/c^4$, $F_S = 0.03 \pm 0.03$, which corresponds to an upper limit of $F_S < 0.04$ at 68% confidence level (CL). The procedure has also been performed in the region $1 < q^2 < 6 \text{ GeV}^2/c^4$, where both F_L and F_S are expected to be enhanced. This gives $F_S = 0.04 \pm 0.04$ and an upper limit of $F_S < 0.07$ at 68% CL. Conservatively, $F_S = 0.07$ is used to estimate a systematic uncertainty on the differential branching fraction and angular analyses. The $B^0 \rightarrow K^{*0} J/\psi$ data has been used to validate the method.

For the differential branching fraction analysis, F_S scales the observed branching fraction by up to 7%. For the angular analysis, F_S dilutes A_{FB} , S_3 and A_9 . The impact on F_L however, is less easy to disentangle. To assess the possible size of a systematic bias,

⁴In the decay $B^0 \rightarrow K^{*0} \mu^+ \mu^-$ there are actually two pairs of amplitudes involved, left- and right-handed longitudinal amplitudes and left- and right-handed S-wave amplitudes (where the handedness refers to the chirality of the dimuon system). In order to exploit the interference and determine F_S it is assumed that the phase difference between the two left-handed amplitudes is the same as the difference between the two right-handed amplitudes, as expected from the expression for the amplitudes in Refs. [39, 40].

426 pseudo-experiments have been carried out generating with, and fitting without, the S-wave
 427 contribution in the likelihood fit. The typical bias on the angular observables due to the
 428 S-wave is $0.01 - 0.03$.

429 7.3.2 Production, detection and direct CP asymmetries

430 If the number of B^0 and \bar{B}^0 decays are not equal in the likelihood fit then the terms in
 431 the angular distribution no longer correspond to pure CP averages or asymmetries. They
 432 instead correspond to admixtures of the two, e.g.

$$S_3^{\text{obs}} \approx S_3 - A_3 (\mathcal{A}_{\text{CP}} + \kappa \mathcal{A}_{\text{P}} + \mathcal{A}_{\text{D}}) , \quad (8)$$

433 where \mathcal{A}_{CP} is the direct CP asymmetry between $B^0 \rightarrow K^{*0} \mu^+ \mu^-$ and $\bar{B}^0 \rightarrow \bar{K}^{*0} \mu^+ \mu^-$
 434 decays, \mathcal{A}_{P} is the production asymmetry between B^0 and \bar{B}^0 mesons, which is diluted by
 435 a factor κ due to $B^0 - \bar{B}^0$ mixing, and \mathcal{A}_{D} is the detection asymmetry between the B^0
 436 and \bar{B}^0 decays (which might be non-zero due to differences in the interaction cross-section
 437 with matter between K^+ and K^- mesons). In practice, the production and detection
 438 asymmetries are small in LHCb and \mathcal{A}_{CP} is measured to be $\mathcal{A}_{\text{CP}} = -0.072 \pm 0.040 \pm 0.05$ [36],
 439 which is consistent with zero. This, combined with the expected small size of the CP
 440 asymmetry or CP -averaged counterparts of the angular observables measured in this
 441 analysis, reduces any systematic bias to < 0.01 (this is neglected in Table 3).

442 8 Forward-backward asymmetry zero-crossing point

443 In the SM, A_{FB} changes sign at a well defined value of q^2 , q_0^2 , whose prediction is largely
 444 free from form-factor uncertainties. It is non-trivial to estimate q_0^2 from the angular fits
 445 to the data in the different q^2 bins. Instead, q_0^2 is estimated by performing a fit to the
 446 q^2 and $K^+ \pi^- \mu^+ \mu^-$ invariant mass distribution of the forward-going ($\cos \theta_\ell > 0$) and
 447 backward-going ($\cos \theta_\ell < 0$) candidates. If $P_{\text{F}}(q^2)$ describes the q^2 dependence of the
 448 forward-going, and $P_{\text{B}}(q^2)$ the backward-going candidates then

$$A_{\text{FB}}(q^2) = \frac{N_{\text{F}} P_{\text{F}}(q^2) - N_{\text{B}} P_{\text{B}}(q^2)}{N_{\text{F}} P_{\text{F}}(q^2) + N_{\text{B}} P_{\text{B}}(q^2)} . \quad (9)$$

449 Here, N_{F} and N_{B} are the total number of forward- and backward-going signal decays,
 450 respectively. The zero-crossing point of A_{FB} is found by solving for the value of q^2 at
 451 which A_{FB} is zero.

452 Using candidates in the range $1.0 < q^2 < 7.8 \text{ GeV}^2/c^4$ and third-order polynomials to
 453 describe the q^2 dependence of the signal and the background, the zero-crossing point is
 454 found to be

$$q_0^2 = 4.9 \pm 0.9 \text{ GeV}^2/c^4 .$$

455 The uncertainty on q_0^2 is determined using a bootstrapping technique [43]. The zero-
 456 crossing point is largely independent of the polynomial order and the q^2 range that is

used. This value is consistent with SM predictions, which are typically in the range $3.9 - 4.4 \text{ GeV}^2/c^4$ [44–46] and have relative uncertainties below the 10% level, example, $q_0^2 = 4.36_{-0.31}^{+0.33} \text{ GeV}^2/c^4$ [45].

The systematic uncertainty on the zero-crossing point of the forward-backward asymmetry is negligible compared to the statistical uncertainty. To generate a large systematic bias, it would be necessary to create an asymmetric acceptance effect in $\cos \theta_\ell$ that is not cancelled when combining B^0 and \bar{B}^0 decays. The combined systematic uncertainty is at the level of $\pm 0.05 \text{ GeV}^2/c^4$.

9 Conclusions

In summary, using a data sample, corresponding to 1.0 fb^{-1} of integrated luminosity, collected by the LHCb experiment in 2011, the differential branching fraction, $d\mathcal{B}/dq^2$, of the decay $B^0 \rightarrow K^{*0} \mu^+ \mu^-$ has been measured in bins of q^2 . Measurements of the angular observables, A_{FB} (A_{T}^{Re}), F_L , S_3 (A_{T}^2) and A_9 have also been performed in the same q^2 bins. These are the most precise measurements of $d\mathcal{B}/dq^2$ and the angular observables to date. A first measurement of the zero-crossing point of the forward-backward asymmetry has also been performed by exploiting the q^2 distribution of forward- and backward-going candidates, with the value $q_0^2 = 4.9 \pm 0.9 \text{ GeV}^2/c^4$. All of the observables are consistent with SM expectations and together put stringent constraints on the contributions from new particles to $b \rightarrow s$ flavour changing neutral current processes.

Acknowledgements

We express our gratitude to our colleagues in the CERN accelerator departments for the excellent performance of the LHC. We thank the technical and administrative staff at the LHCb institutes. We acknowledge support from CERN and from the national agencies: CAPES, CNPq, FAPERJ and FINEP (Brazil); NSFC (China); CNRS/IN2P3 and Region Auvergne (France); BMBF, DFG, HGF and MPG (Germany); SFI (Ireland); INFN (Italy); FOM and NWO (The Netherlands); SCSR (Poland); ANCS/IFA (Romania); MinES, Rosatom, RFBR and NRC “Kurchatov Institute” (Russia); MinECo, XuntaGal and GENCAT (Spain); SNSF and SER (Switzerland); NAS Ukraine (Ukraine); STFC (United Kingdom); NSF (USA). We also acknowledge the support received from the ERC under FP7. The Tier1 computing centres are supported by IN2P3 (France), KIT and BMBF (Germany), INFN (Italy), NWO and SURF (The Netherlands), PIC (Spain), GridPP (United Kingdom). We are thankful for the computing resources put at our disposal by Yandex LLC (Russia), as well as to the communities behind the multiple open source software packages that we depend on.

Appendix

A Angular basis

The angular basis used in this paper is illustrated in Fig. 6. The angle θ_ℓ is defined as the angle between the direction of the μ^+ (μ^-) in the dimuon rest frame and the direction of the dimuon in the B^0 (\bar{B}^0) rest frame. The angle θ_K is defined as the angle between the direction of the kaon in the K^{*0} (\bar{K}^{*0}) rest frame and the direction of the K^{*0} (\bar{K}^{*0}) in the B^0 (\bar{B}^0) rest frame. The angle ϕ is the angle between the plane containing the μ^+ and μ^- and the plane containing the kaon and pion from the K^{*0} . Explicitly, $\cos \theta_\ell$ and $\cos \theta_K$ are defined as

$$\cos \theta_\ell = \left(\hat{p}_{\mu^+}^{(\mu^+\mu^-)} \cdot \hat{p}_{\mu^+\mu^-}^{(B^0)} \right) = \left(\hat{p}_{\mu^+}^{(\mu^+\mu^-)} \cdot \left(-\hat{p}_{B^0}^{(\mu^+\mu^-)} \right) \right), \quad (10)$$

$$\cos \theta_K = \left(\hat{p}_{K^+}^{(K^{*0})} \cdot \hat{p}_{K^{*0}}^{(B^0)} \right) = \left(\hat{p}_{K^+}^{(K^{*0})} \cdot \left(-\hat{p}_{B^0}^{(K^{*0})} \right) \right) \quad (11)$$

for the B^0 and

$$\cos \theta_\ell = \left(\hat{p}_{\mu^-}^{(\mu^+\mu^-)} \cdot \hat{p}_{\mu^+\mu^-}^{(\bar{B}^0)} \right) = \left(\hat{p}_{\mu^-}^{(\mu^+\mu^-)} \cdot \left(-\hat{p}_{\bar{B}^0}^{(\mu^+\mu^-)} \right) \right), \quad (12)$$

$$\cos \theta_K = \left(\hat{p}_{K^-}^{(K^{*0})} \cdot \hat{p}_{K^{*0}}^{(\bar{B}^0)} \right) = \left(\hat{p}_{K^-}^{(K^{*0})} \cdot \left(-\hat{p}_{\bar{B}^0}^{(K^{*0})} \right) \right) \quad (13)$$

for the \bar{B}^0 decay. The definition of the angle ϕ is given by

$$\cos \phi = \left(\left(\hat{p}_{\mu^+}^{(B^0)} \times \hat{p}_{\mu^-}^{(B^0)} \right) \cdot \left(\hat{p}_{K^+}^{(B^0)} \times \hat{p}_{\pi^-}^{(B^0)} \right) \right), \quad (14)$$

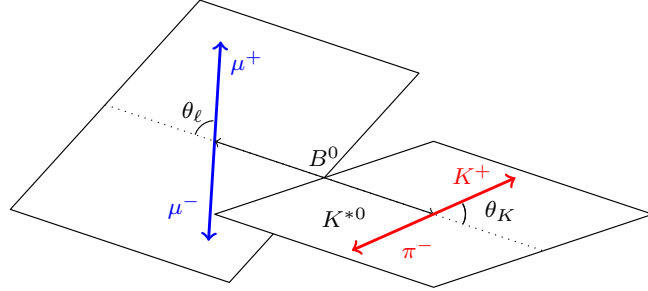
$$\sin \phi = \left(\left(\hat{p}_{\mu^+}^{(B^0)} \times \hat{p}_{\mu^-}^{(B^0)} \right) \times \left(\hat{p}_{K^+}^{(B^0)} \times \hat{p}_{\pi^-}^{(B^0)} \right) \right) \cdot \hat{p}_{K^{*0}}^{(B^0)} \quad (15)$$

for the B^0 and

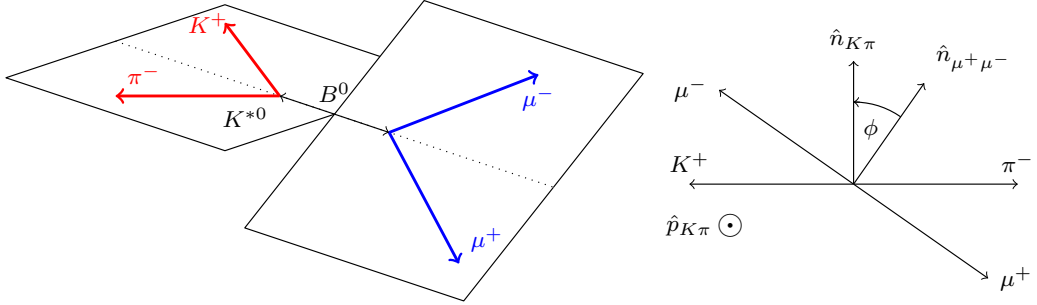
$$\cos \phi = \left(\left(\hat{p}_{\mu^-}^{(\bar{B}^0)} \times \hat{p}_{\mu^+}^{(\bar{B}^0)} \right) \cdot \left(\hat{p}_{K^-}^{(\bar{B}^0)} \times \hat{p}_{\pi^+}^{(\bar{B}^0)} \right) \right), \quad (16)$$

$$\sin \phi = - \left(\left(\hat{p}_{\mu^-}^{(\bar{B}^0)} \times \hat{p}_{\mu^+}^{(\bar{B}^0)} \right) \times \left(\hat{p}_{K^-}^{(\bar{B}^0)} \times \hat{p}_{\pi^+}^{(\bar{B}^0)} \right) \right) \cdot \hat{p}_{\bar{K}^{*0}}^{(\bar{B}^0)} \quad (17)$$

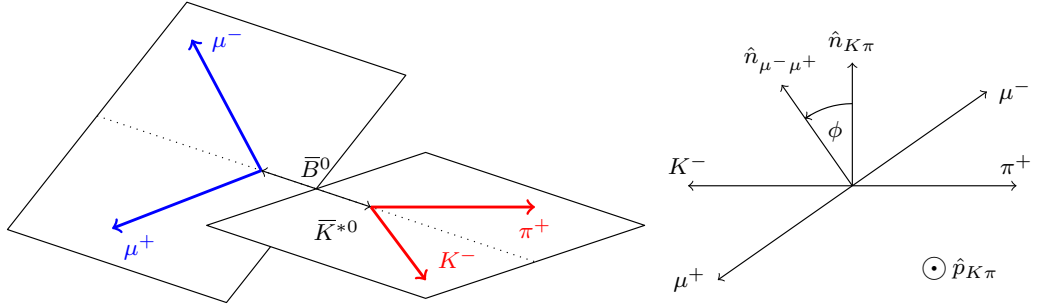
for the \bar{B}^0 decay. The $\hat{p}_X^{(Y)}$ are unit vectors describing the direction of a particle X in the rest frame of the system Y . In every case the particle momenta are first boosted to the B^0 (or \bar{B}^0) rest frame. In this basis, the angular definition for the \bar{B}^0 decay is a CP transformation of that for the B^0 decay.



(a) θ_K and θ_ℓ definitions for the B^0 decay



(b) ϕ definition for the B^0 decay



(c) ϕ definition for the \bar{B}^0 decay

Figure 6: Graphical representation of the angular basis used for $B^0 \rightarrow K^{*0} \mu^+ \mu^-$ and $\bar{B}^0 \rightarrow \bar{K}^{*0} \mu^+ \mu^-$ decays in this paper. The notation \hat{n}_{ab} is used to represent the normal to the plane containing particles a and b in the B^0 (or \bar{B}^0) rest frame. An explicit description of the angular basis is given in the text.

B Angular distribution at large recoil

An explicit example of the dilution of the angular observables that comes from the threshold terms is provided below for A_T^2 . Sensitivity to A_T^2 comes through the term in Eq. 1 with $\sin^2 \theta_\ell \sin^2 \theta_K \cos 2\phi$ angular dependence. In the limit $q^2 \gg m_\mu^2$, this term is simply

$$\frac{1}{2} (1 - F_L(q^2)) A_T^2(q^2) \sin^2 \theta_\ell \sin^2 \theta_K \cos 2\phi \quad (18)$$

and the differential decay width is

$$\frac{d\Gamma}{dq^2} = |A_{0,L}|^2 + |A_{\parallel,L}|^2 + |A_{\perp,L}|^2 + |A_{0,R}|^2 + |A_{\parallel,R}|^2 + |A_{\perp,R}|^2, \quad (19)$$

where A_0 , A_\parallel and A_\perp are the K^{*0} spin-amplitudes and the L/R index refers to the chirality of the lepton current (see for example Ref. [1]). If $q^2 \lesssim 1 \text{ GeV}^2/c^4$, these expressions are modified to

$$\frac{1}{2} \left[\frac{1 - 4m_\mu^2/q^2}{1 + 2m_\mu^2/q^2} \right] (1 - F_L(q^2)) A_T^2(q^2) \sin^2 \theta_\ell \sin^2 \theta_K \cos 2\phi \quad (20)$$

and

$$\frac{d\Gamma}{dq^2} = [1 + 2m_\mu^2/q^2] (|A_{0,L}|^2 + |A_{\parallel,L}|^2 + |A_{\perp,L}|^2 + |A_{0,R}|^2 + |A_{\parallel,R}|^2 + |A_{\perp,R}|^2). \quad (21)$$

In an infinitesimal window of q^2 , the difference between an experimental measurement of A_T^2 , $A_T^{2 \text{ exp}}$, in which the threshold terms are neglected and the value of A_T^2 defined in literature is

$$\frac{A_T^{2 \text{ exp}}}{A_T^2} = \left[\frac{1 - 4m_\mu^2/q^2}{1 + 2m_\mu^2/q^2} \right]. \quad (22)$$

Unfortunately, in a wider q^2 window, the q^2 dependence of F_L , A_T^2 and the threshold terms needs to be considered and it becomes less straightforward to estimate the dilution due to the threshold terms. If A_T^2 is constant over the q^2 window,

$$\frac{A_T^{2 \text{ exp}}}{A_T^2} = \frac{\int_{q_{\min}^2}^{q_{\max}^2} \frac{d\Gamma}{dq^2} \left[\frac{1 - 4m_\mu^2/q^2}{1 + 2m_\mu^2/q^2} \right] [1 - F_L(q^2)] dq^2}{\int_{q_{\min}^2}^{q_{\max}^2} \frac{d\Gamma}{dq^2} [1 - F_L(q^2)] dq^2}. \quad (23)$$

In practice the integration in Eq. 23 can be replaced by a sum over the signal events in the q^2 window

$$\frac{A_{\text{T}}^2{}^{\text{exp}}}{A_{\text{T}}^2} = \frac{\sum_{i=0}^N \left[\frac{1-4m_{\mu}^2/q_i^2}{1+2m_{\mu}^2/q_i^2} \right] (1 - F_{\text{L}}(q_i^2)) \omega_i}{\sum_{i=0}^N (1 - F_{\text{L}}(q_i^2)) \omega_i}, \quad (24)$$

where ω_i is a weight applied to the i^{th} candidate to account for the detector and selection acceptance and the background in the q^2 window.

Correction factors for the other observables can be similarly defined if it is assumed that they are constant over the q^2 window. In the case of A_{FB} (and A_{T}^{Re}) that are expected to exhibit a strong q^2 dependence, the q^2 dependence of the observable needs to be considered.

References

- [1] W. Altmannshofer *et al.*, *Symmetries and asymmetries of $B \rightarrow K^* \mu^+ \mu^-$ decays in the Standard Model and beyond*, JHEP **01** (2009) 019, [arXiv:0811.1214](#).
- [2] C. Bobeth, G. Hiller, and G. Piranishvili, *CP asymmetries in $\bar{B} \rightarrow \bar{K}^*(\rightarrow \bar{K} \pi) \bar{\ell} \ell$ and untagged $\bar{B}_s, B_s \rightarrow \phi(\rightarrow K^+ K^-) \bar{\ell} \ell$ decays at NLO*, JHEP **07** (2008) 106, [arXiv:0805.2525](#).
- [3] A. Ali, P. Ball, L. T. Handoko, and G. Hiller, *Comparative study of the decays $B \rightarrow (K, K^*) \ell^+ \ell^-$ in the standard model and supersymmetric theories*, Phys. Rev. **D61** (2000) 074024, [arXiv:hep-ph/9910221](#).
- [4] F. Krüger and J. Matias, *Probing new physics via the transverse amplitudes of $B^0 \rightarrow K^{*0}(\rightarrow K^- \pi^+) \ell^+ \ell^-$ at large recoil*, Phys. Rev. **D71** (2005) 094009, [arXiv:hep-ph/0502060](#).
- [5] D. Becirevic and E. Schneider, *On transverse asymmetries in $B \rightarrow K^* \ell^+ \ell^-$* , Nucl. Phys. **B854** (2012) 321, [arXiv:1106.3283](#).
- [6] LHCb collaboration, R. Aaij *et al.*, *Differential branching fraction and angular analysis of the decay $B^0 \rightarrow K^{*0} \mu^+ \mu^-$* , Phys. Rev. Lett. **108** (2012) 181806, [arXiv:1112.3515](#).
- [7] BaBar collaboration, B. Aubert *et al.*, *Measurements of branching fractions, rate asymmetries, and angular distributions in the rare decays $B \rightarrow K \ell^+ \ell^-$ and $B \rightarrow K^* \ell^+ \ell^-$* , Phys. Rev. **D73** (2006) 092001, [arXiv:hep-ex/0604007](#).
- [8] Belle collaboration, J.-T. Wei *et al.*, *Measurement of the differential branching fraction and forward-backward asymmetry for $B \rightarrow K^{(*)} \ell^+ \ell^-$* , Phys. Rev. Lett. **103** (2009) 171801, [arXiv:0904.0770](#).
- [9] CDF collaboration, T. Aaltonen *et al.*, *Measurements of the angular distributions in the decays $B \rightarrow K^{(*)} \mu^+ \mu^-$ at CDF*, Phys. Rev. Lett. **108** (2012) 081807, [arXiv:1108.0695](#).

- [10] LHCb collaboration, A. A. Alves Jr. *et al.*, *The LHCb detector at the LHC*, JINST **3** (2008) S08005.
- [11] M. Adinolfi *et al.*, *Performance of the LHCb RICH detector at the LHC*, arXiv:1211.6759, submitted to Eur. Phys. J. C.
- [12] R. Aaij *et al.*, *The LHCb trigger and its performance*, arXiv:1211.3055, to appear in JINST.
- [13] T. Sjöstrand, S. Mrenna, and P. Skands, *PYTHIA 6.4 physics and manual*, JHEP **05** (2006) 026, arXiv:hep-ph/0603175.
- [14] I. Belyaev *et al.*, *Handling of the generation of primary events in GAUSS, the LHCb simulation framework*, Nuclear Science Symposium Conference Record (NSS/MIC) **IEEE** (2010) 1155.
- [15] D. J. Lange, *The EvtGen particle decay simulation package*, Nucl. Instrum. Meth. **A462** (2001) 152.
- [16] P. Golonka and Z. Was, *PHOTOS Monte Carlo: a precision tool for QED corrections in Z and W decays*, Eur. Phys. J. **C45** (2006) 97, arXiv:hep-ph/0506026.
- [17] GEANT4 collaboration, J. Allison *et al.*, *Geant4 developments and applications*, IEEE Trans. Nucl. Sci. **53** (2006) 270; GEANT4 collaboration, S. Agostinelli *et al.*, *GEANT4: a simulation toolkit*, Nucl. Instrum. Meth. **A506** (2003) 250.
- [18] M. Clemencic *et al.*, *The LHCb simulation application, GAUSS: design, evolution and experience*, J. of Phys: Conf. Ser. **331** (2011) 032023.
- [19] L. Breiman, J. H. Friedman, R. A. Olshen, and C. J. Stone, *Classification and regression trees*, Wadsworth international group, Belmont, California, USA, 1984.
- [20] Y. Freund and R. E. Schapire, *A decision-theoretic generalization of on-line learning and an application to boosting*, Jour. Comp. and Syst. Sc. **55** (1997) 119.
- [21] LHCb collaboration, R. Aaij *et al.*, *Measurement of the fragmentation fraction ratio f_s/f_d and its dependence on B meson kinematics*, JHEP **04** (2013) 001, arXiv:1301.5286.
- [22] T. Skwarnicki, *A study of the radiative cascade transitions between the Upsilon-prime and Upsilon resonances*, PhD thesis, Institute of Nuclear Physics, Krakow, 1986, DESY-F31-86-02.
- [23] Particle Data Group, J. Beringer *et al.*, *Review of particle physics*, Phys. Rev. **D86** (2012) 010001.

- [24] BaBar collaboration, B. Aubert *et al.*, *Measurement of branching fractions and charge asymmetries for exclusive B decays to charmonium*, Phys. Rev. Lett. **94** (2005) 141801, [arXiv:hep-ex/0412062](#).
- [25] C. Bobeth, G. Hiller, and D. van Dyk, *More benefits of semileptonic rare B decays at low recoil: CP violation*, JHEP **07** (2011) 067, [arXiv:1105.0376](#).
- [26] S. Descotes-Genon, T. Hurth, J. Matias, and J. Virto, *Optimizing the basis of $B \rightarrow K^* \ell^+ \ell^-$ observables in the full kinematic range*, [arXiv:1303.5794](#).
- [27] M. Beneke, T. Feldmann, and D. Seidel, *Systematic approach to exclusive $B \rightarrow V \ell^+ \ell^-$, $V \gamma$ decays*, Nucl. Phys. **B612** (2001) 25, [arXiv:hep-ph/0106067](#).
- [28] B. Grinstein and D. Pirjol, *Exclusive rare $B \rightarrow K^* \ell^+ \ell^-$ decays at low recoil: controlling the long-distance effects*, Phys. Rev. **D70** (2004) 114005, [arXiv:hep-ph/0404250](#).
- [29] M. Beylich, G. Buchalla, and T. Feldmann, *Theory of $B \rightarrow K^{(*)} \ell^+ \ell^-$ decays at high q^2 : OPE and quark-hadron duality*, Eur. Phys. J. **C71** (2011) 1635, [arXiv:1101.5118](#).
- [30] P. Ball and R. Zwicky, *$B_{d,s} \rightarrow \rho, \omega, K^*, \phi$ decay form factors from light-cone sum rules reexamined*, Phys. Rev. D **71** (2005) 014029, [arXiv:hep-ph/0412079](#).
- [31] U. Egede *et al.*, *New observables in the decay mode $\bar{B}_d \rightarrow \bar{K}^{*0} \ell^+ \ell^-$* , JHEP **11** (2008) 032, [arXiv:0807.2589](#).
- [32] S. Jager and J. M. Camalich, *On $B \rightarrow V \ell \ell$ at small dilepton invariant mass, power corrections, and new physics*, [arXiv:1212.2263](#).
- [33] J. Matias, F. Mescia, M. Ramon, and J. Virto, *Complete anatomy of $\bar{B}_d \rightarrow \bar{K}^{*0} (\rightarrow K \pi) \ell^+ \ell^-$ and its angular distribution*, JHEP **04** (2012) 104, [arXiv:1202.4266](#).
- [34] G. J. Feldman and R. D. Cousins, *Unified approach to the classical statistical analysis of small signals*, Phys. Rev. **D57** (1998) 3873, [arXiv:physics/9711021](#).
- [35] B. Sen, M. Walker, and M. Woodroffe, *On the unified method with nuisance parameters*, Statistica Sinica **19** (2009) 301.
- [36] LHCb collaboration, R. Aaij *et al.*, *Measurement of the CP asymmetry in $B^0 \rightarrow K^{*0} \mu^+ \mu^-$ decays*, Phys. Rev. Lett. **110** (2012) 031801, [arXiv:1210.4492](#).
- [37] BaBar collaboration, B. Aubert *et al.*, *Measurement of decay amplitudes of $B^0 \rightarrow J/\psi K^{*0}$, $\psi(2S) K^{*0}$, and $\chi_{c1} K^{*0}$ with an angular analysis*, Phys. Rev. **D76** (2007) 031102, [arXiv:0704.0522](#).
- [38] LHCb collaboration, *Differential branching fraction and angular analysis of the decay $B_s^0 \rightarrow \phi \mu^+ \mu^-$* , LHCb-PAPER-2013-017. In preparation.

- 618 [39] C.-D. Lu and W. Wang, *Analysis of $B \rightarrow K_J^*(\rightarrow K\pi)\mu^+\mu^-$ in the higher kaon*
619 *resonance region*, Phys. Rev. **D85** (2012) 034014, [arXiv:1111.1513](#).
- 620 [40] D. Becirevic and A. Tayduganov, *Impact of $B \rightarrow K_0^*\ell^+\ell^-$ on the new physics search*
621 *in $B \rightarrow K^*\ell^+\ell^-$ decay*, Nucl. Phys. **B868** (2013) 368, [arXiv:1207.4004](#).
- 622 [41] T. Blake, U. Egede, and A. Shires, *The effect of S -wave interference on the $B^0 \rightarrow$*
623 *$K^{*0}\ell^+\ell^-$ angular observables*, JHEP **03** (2013) 027, [arXiv:1210.5279](#).
- 624 [42] J. Matias, *On the S -wave pollution of $B \rightarrow K^*l^+l^-$ observables*, Phys. Rev. **D86**
625 (2012) 094024, [arXiv:1209.1525](#).
- 626 [43] B. Efron, *Bootstrap methods: Another look at the jackknife*, Ann. Statist. **7** (1979) 1.
- 627 [44] C. Bobeth, G. Hiller, D. van Dyk, and C. Wacker, *The decay $\bar{B} \rightarrow \bar{K}\ell^+\ell^-$ at low*
628 *hadronic recoil and model-independent $\Delta B = 1$ constraints*, JHEP **01** (2012) 107,
629 [arXiv:1111.2558](#).
- 630 [45] M. Beneke, T. Feldmann, and D. Seidel, *Exclusive radiative and electroweak $b \rightarrow d$ and*
631 *$b \rightarrow s$ penguin decays at NLO*, Eur. Phys. J. **C41** (2005) 173, [arXiv:hep-ph/0412400](#).
- 632 [46] A. Ali, G. Kramer, and G.-h. Zhu, *$B \rightarrow K^*\ell^+\ell^-$ decay in soft-collinear effective*
633 *theory*, Eur. Phys. J. **C47** (2006) 625, [arXiv:hep-ph/0601034](#).